## Supplementary Information

# Reductive Electron Redistribution Enables Ultrafast Charging Magnesium Batteries

Wenbin Wang, Hongyu Zhang*, Miao Guo, Chaoqun Li, Xian Zhou, Guanglin Xia, Xuebin Yu[1,]**

Department of Materials Science, Fudan University, China

Present address: 220 Handan Road, Shanghai, China

*Correspondence: zhang_hongyu@fudan.edu.cn

**Correspondence: yuxuebin@fudan.edu.cn

## Figures S1–S66, and Table S1-S11.

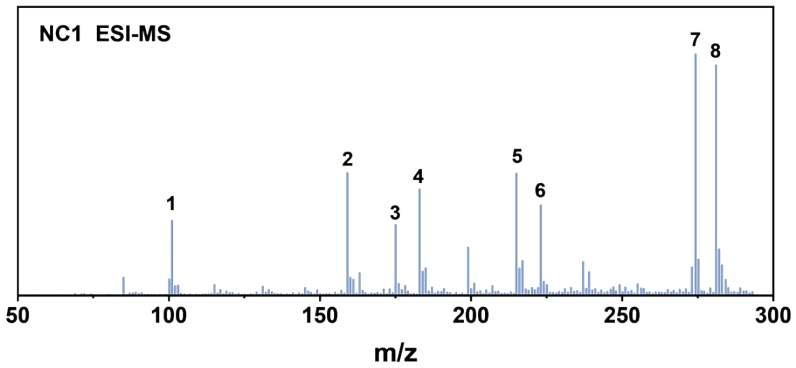


**Figure S1.** Electrospray ionization mass spectrometry (ESI-MS) of $Mg(TFSI)_2$-NC1-DME. In NC1 electrolyte, monoamine molecules are characterized in the solvated $Mg^{2+}$, indicating the simultaneous presence of monoamine cations and molecules in the electrolyte.

1. $Mg(DME)_2^{2+}$, m/z≈101;
2. $[NC1\text{-}CH_3(OCH_2CH_2)_2CH_3]^+$, m/z≈160;
3. $[Mg(DME)(NC1)_2]^+$, m/z≈175;
4. $[MgCl(NC1)(DME)]^+$, m/z≈181;
5. $[MgCl(NC1)\text{-}CH_3(OCH_2CH_2)_2CH_3)]^+$, m/z≈220;
6. $[Mg(DME)_3(NC1)_5]^{2+}$, m/z≈225;
7. $[MgCl(NC1)(DME)_2]^+$, m/z≈274;
8. $[Mg(DME)_6]^{2+}$, m/z≈282.

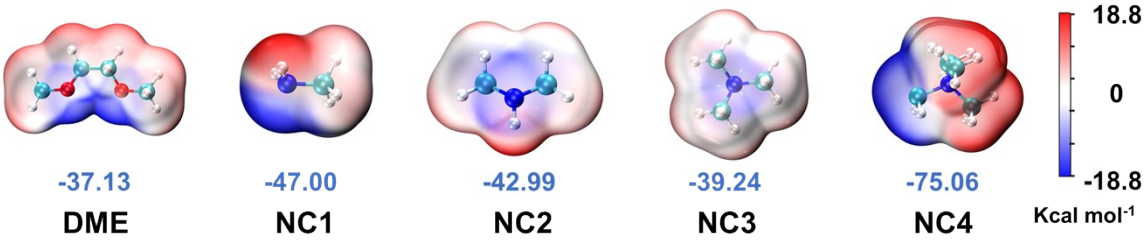


**Figure S2.** Calculated electrostatic potential plots and the most negative electrostatic potential of monoamine molecules and DME molecule. The red, grey, blue and white balls refer to O, C, N and H atoms, respectively.

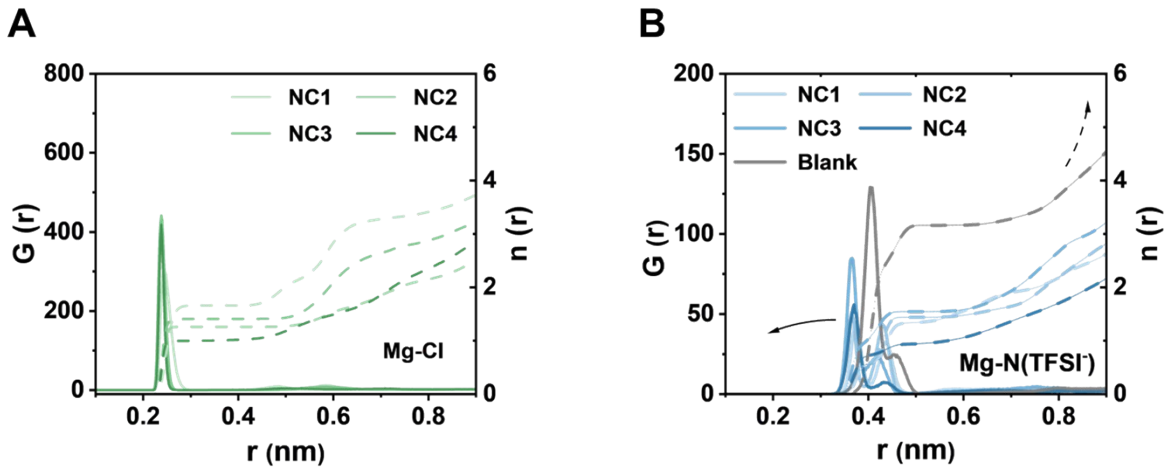


**Figure S3.** Radical distribution function of $Cl^-$ (A) and N in $TFSI^-$ (B) calculated by c-MD.

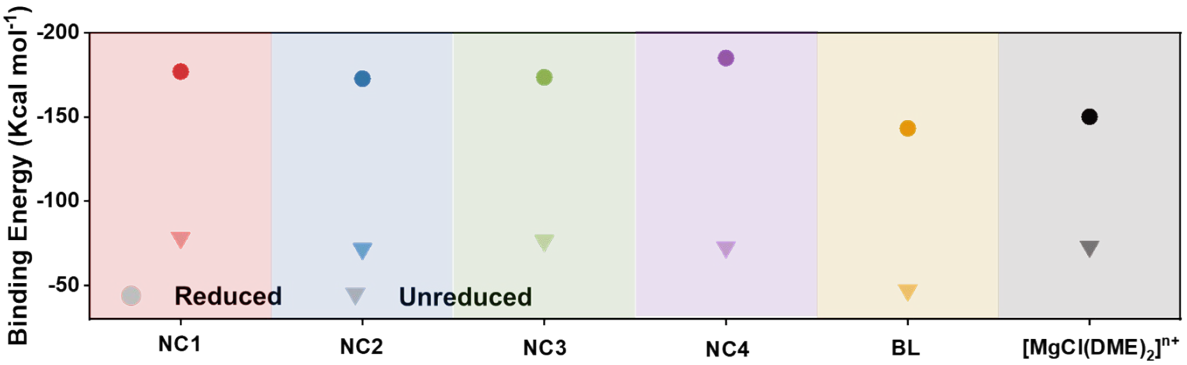


**Figure S4.** The calculated binding energies of solvation sheath before and after obtaining a reductive electron. The solvation sheath in the blank group is $Mg(DME)_3^{2+}$, while a DME molecule is replaced in other groups. Relatively to the blank group, the binding energy of experimental groups is higher, especially in the reduced states.

Relatively to the blank solvation sheath [$Mg(DME)_3^{2+}$], the solvation sheath is more stable when monoamines are involved.

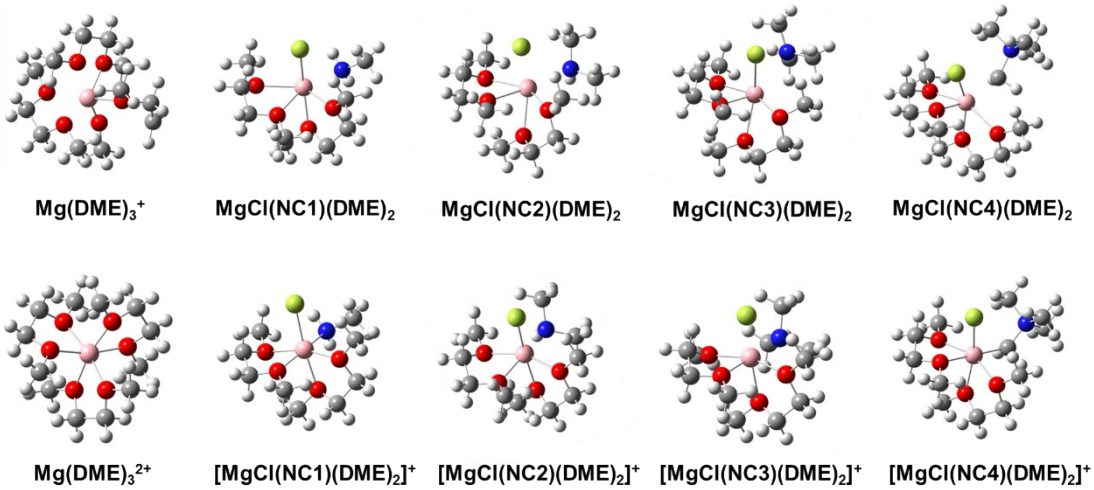


**Figure S5.** The calculated structure of reduced (up) and unreduced (down) solvation sheath. The red, grey, green, blue and white ball represents O, C, Cl, N and H atom, respectively.

| | 0 ps | 0.1 ps | 0.2 ps | 0.5 ps |
|---|---|---|---|---|
| NC2(r) | 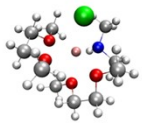 |  | 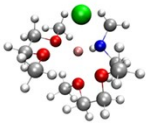 | 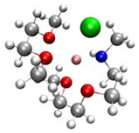 |
| NC3(r) | 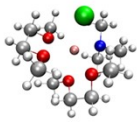 | 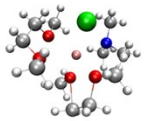 | 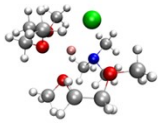 | 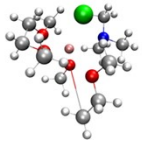 |
| NC4(r) | 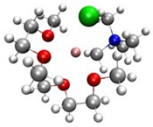 | 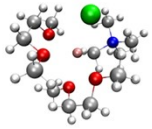 | 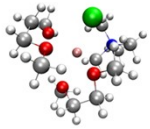 | 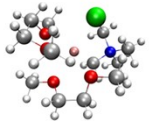 |

**Figure S6.** Ab initio molecular dynamics simulation process of the $[Mg(NCx)(DME)_2]^+$ (x=2-4). The "r" represents the "reduced" solvation sheath.

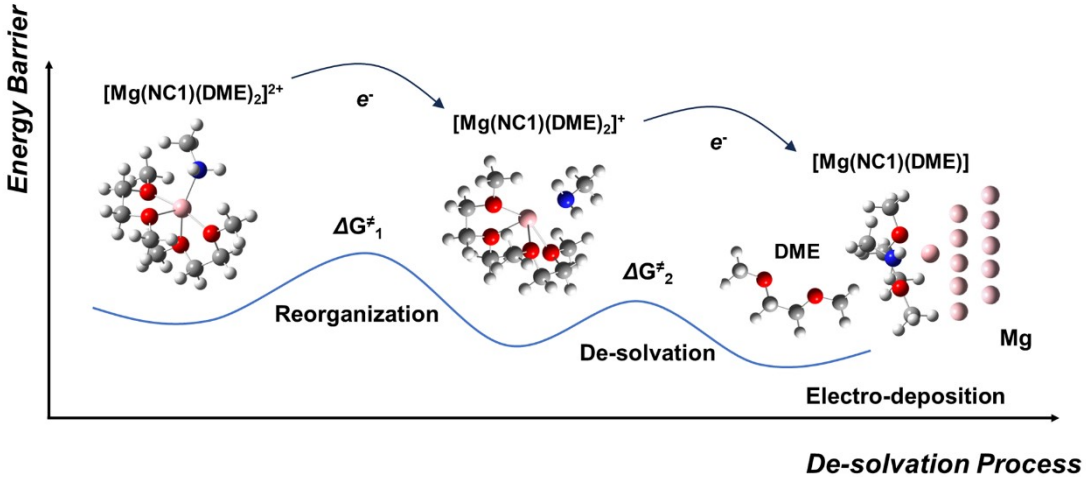


**Figure S7.** The schematic illustration of the whole de-solvation and deposition process of $[Mg(NC1)(DME)_2]^{2+}$.

During the de-solvation process, the solvation sheath first receives a reductive electron and rearrange its structure, and then a DME molecule is de-solvated. After that, the interaction between Mg ion and solvating molecules is lower, thus facilitating further de-solvation. Next, the structure receives another electron and reorganize again, and then Mg is deposited on the surface of Mg anode naturally. The energy barrier of subsequent steps is much lower than that of the first steps, and therefore not discussed in detail.

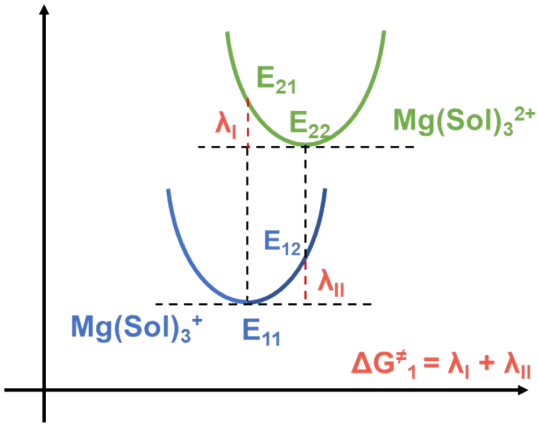


**Figure S8.** Four-point mothed demonstration of the calculating reorganization energy. The green and blue curve refer to the solvation sheath before and after capturing a reductive electron, respectively.

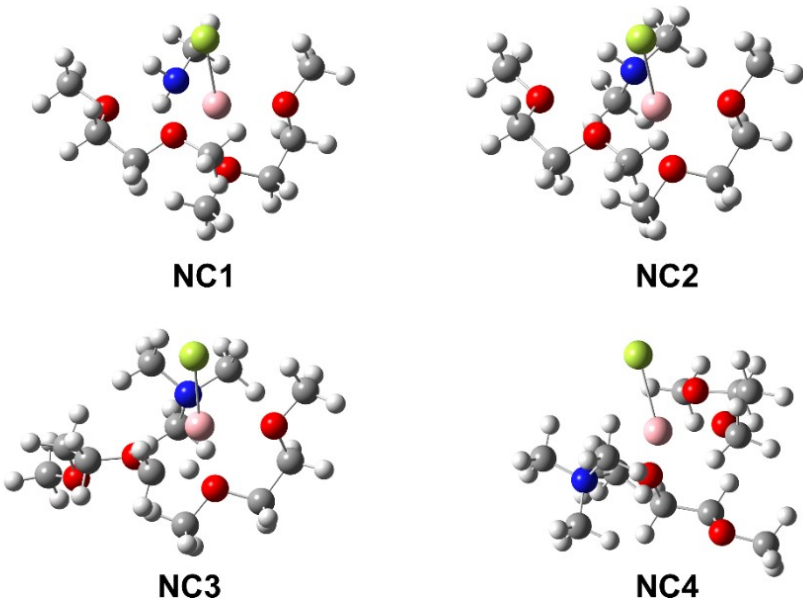


**Figure S9.** The solvation sheath structure when DME molecules are de-solvated firstly. The snapshots illustrate the moment when one coordination site becomes detached.

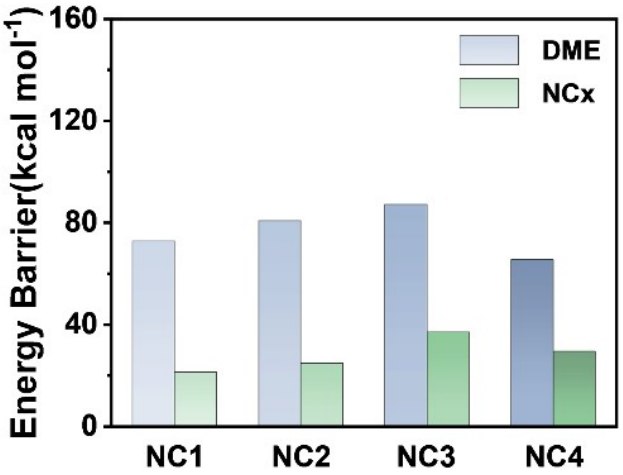


**Figure S10.** The energy barrier of de-solvation process when DME and monoamines detach first.

As it shows, the de-solvation energy of monoamines is much higher than that of DME molecules in all the experiment groups. It implies DME tend to be de-solvated preferentially.

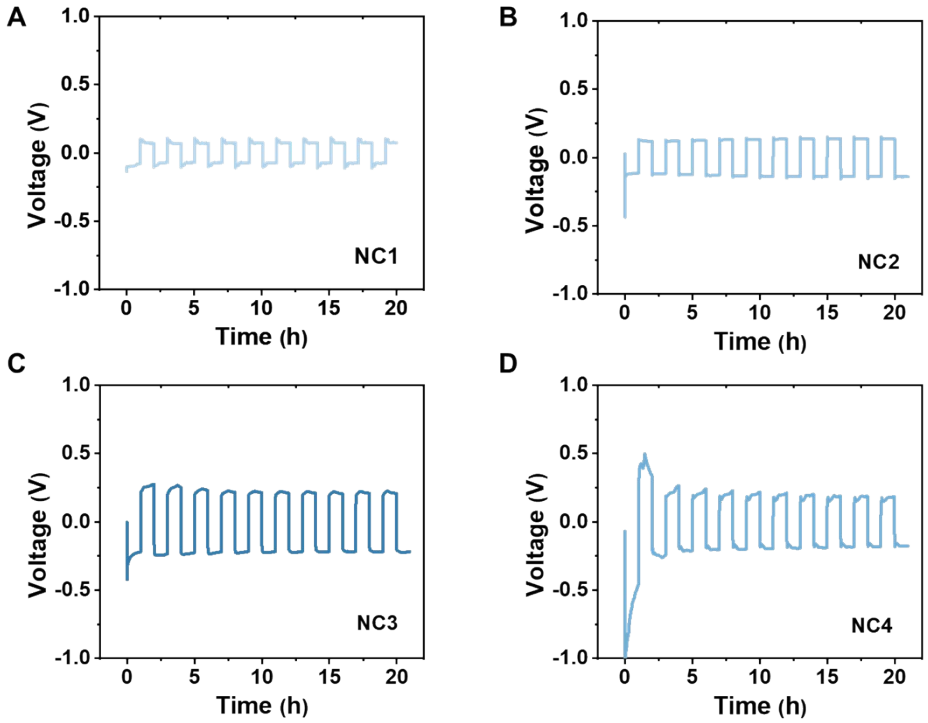


**Figure S11.** The voltage curves of Mg||Mg symmetry cells with the electrolyte of (A) NC1, (B) NC2, (C) NC3 and (D) NC4 at 0.1 mA $cm^{-2}$ and 0.1 mAh $cm^{-2}$, respectively.

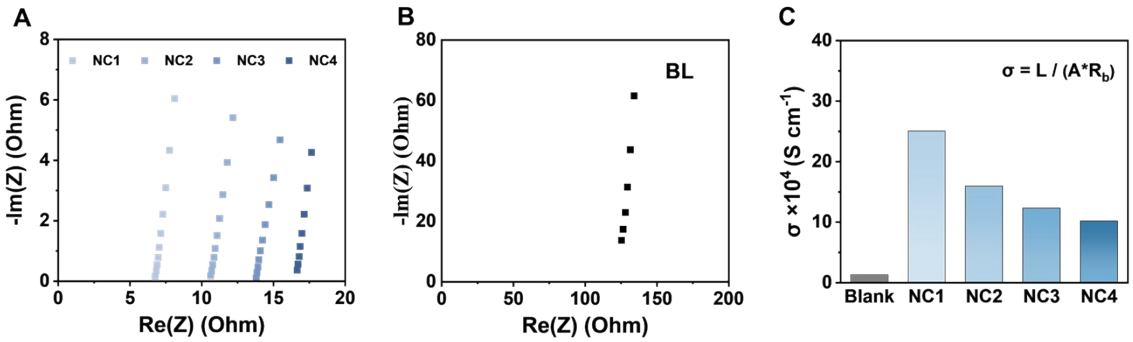


**Figure S12.** The potentiostatic electrochemical impedance spectroscopy (PEIS) of SS||SS symmetry cells with the electrolyte of (A) experimental group and (B) blank group. The $R_b$ is estimated by the intercept of the fitted curve with the X-axis. **C,** The calculated ionic conductivity of the blank and experimental groups. All the calculating details are presented in Table S5.

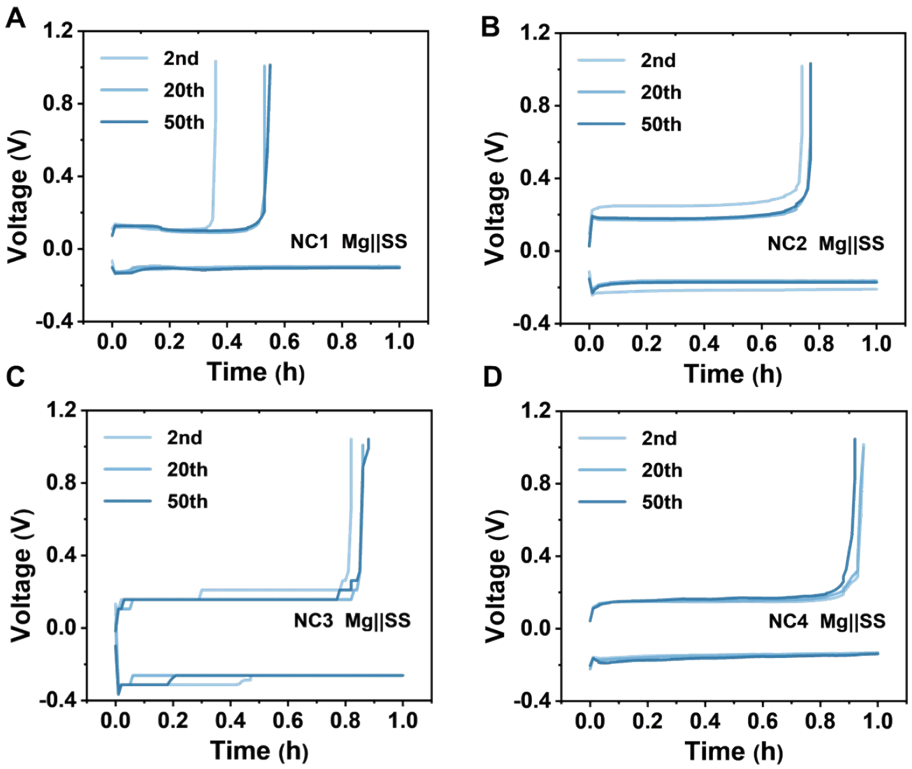


**Figure S13.** The voltage profiles of the Mg||SS half cells in CE tests with the electrolyte of (A) NC1, (B) NC2, (C) NC3 and (D) NC4, respectively. Overall, the CE improves from NC1 to NC4. For each electrolyte, the CE improves slightly from the 2$^{nd}$ cycle to the 20$^{th}$ cycle, which could be regarded as the conditioning process. The 20$^{th}$ charging profile resembles that of 50$^{th}$, implying the stability of these electrolytes.

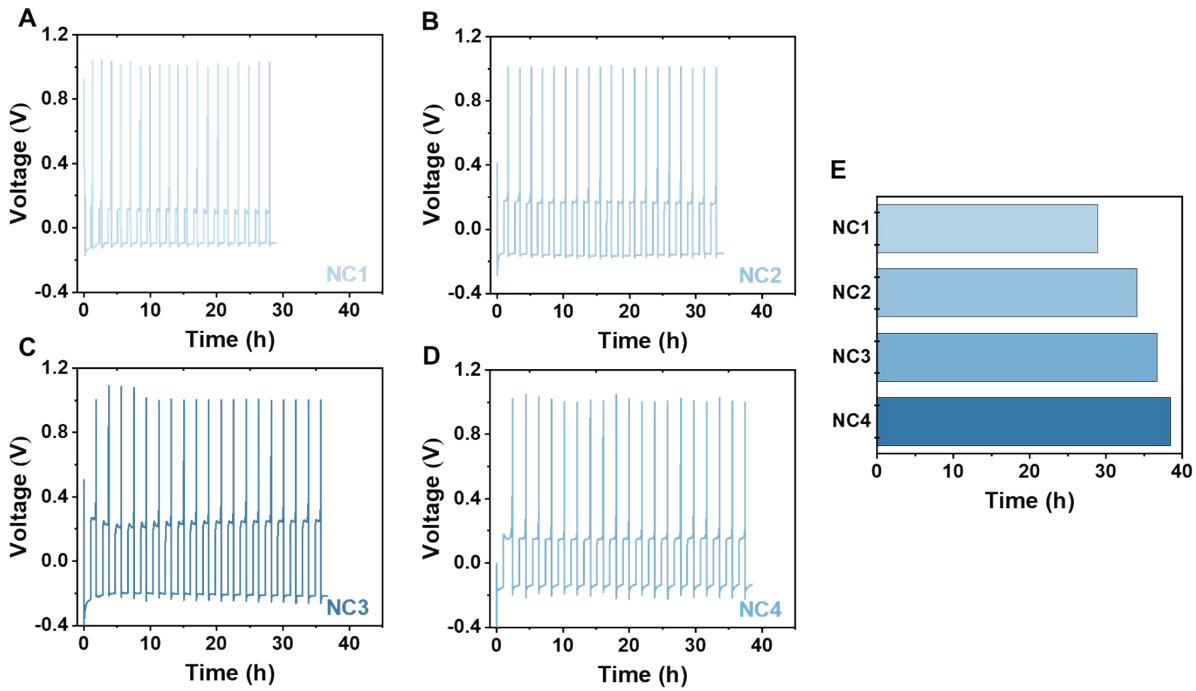


**Figure S14.** 20-cycle voltage curves of Mg||SS half cells with the electrolyte of (A) NC1, (B) NC2, (C) NC3 and (D) NC4 group tested at 0.1 mA $cm^{-2}$ and 0.1 mAh $cm^{-2}$ (Mg plating)/1 V (Mg stripping). (E) The total spending time for 20 cycles in each group. The higher coulombic efficiency is, the longer time it takes for 20 cycles. If the CE achieves totally 100%, the cycling time would be 40 h.

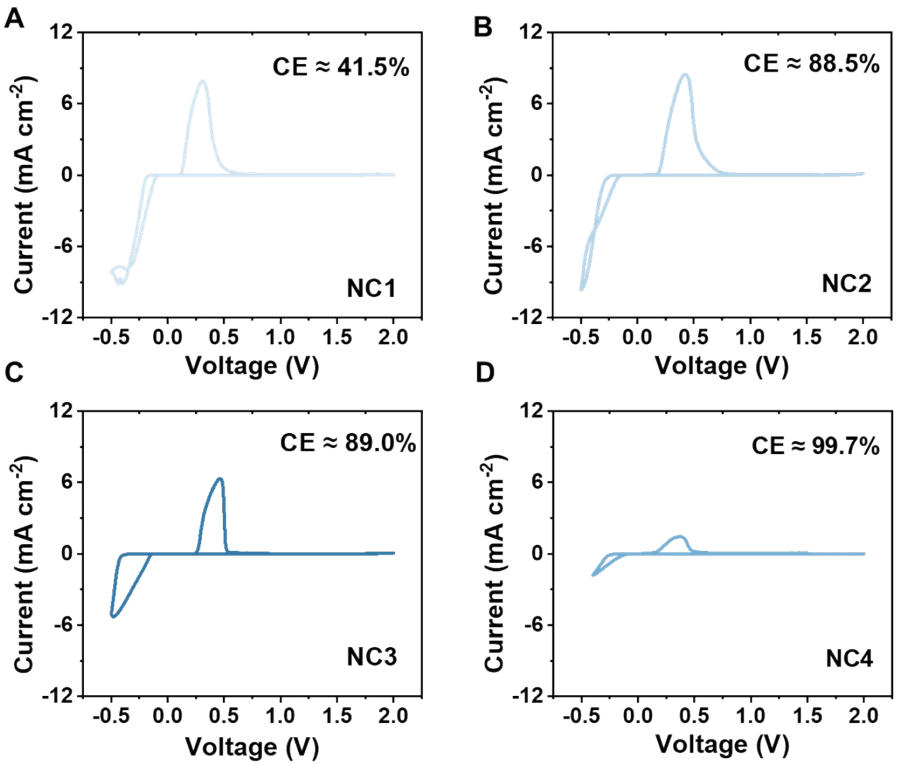


**Figure S15.** The coulombic efficiency of Mg||SS half cells with the electrolyte of (A) NC1, (B) NC2, (C) NC3 and (D) NC4 measured by CV tests at 0.1 mA $cm^{-2}$ and 0.1 mAh $cm^{-2}$, respectively.

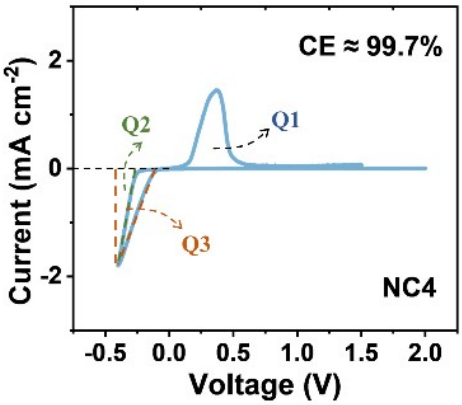


**Figure. S16.** The CV curves of Mg||SS cells with NC4 electrolyte.

The CE is tested in a well-conditioned Mg||stainless steel (Mg||SS) cell. To begin with, the potential is swept cathodically to deposit Mg on the surface of SS. Once the preset cutoff potential (–0.5 V) is reached, the scan direction is reversed to strip the deposited Mg. The anodic scan is stopped at 1.0 V, when Mg stripping is assumed to be complete. The integrated areas between the charge-discharge curves and the horizontal axis are denoted as Q1, Q2 and Q3, respectively. These values represent the quantity of Mg plated/stripped in the electrochemical reactions. The CE is then calculated as Q1/(Q2+Q3). With this method, the CE of Mg||SS half cells with NC4 electrolytes are close to 100%.

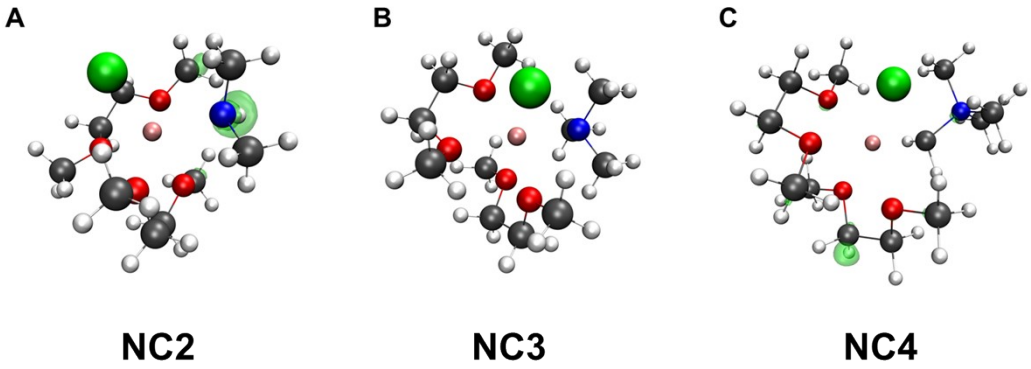


**Figure S17.** Electron density difference plots between reduced/unreduced solvation sheath in (A) NC2, (B) NC3 and (C) NC4. The red, grey, green, blue and white balls refer to O, C, Cl, N and H atoms, respectively.

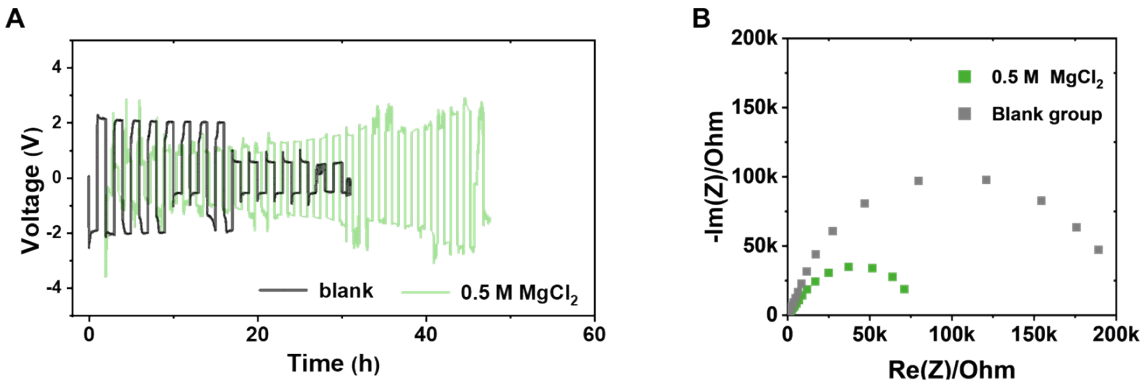


**Figure S18.** (A) The voltage profiles and (B) The PEIS plots of the Mg||Mg symmetry cells with the electrolyte of $Mg(TFSI)_2$-DME and $Mg(TFSI)_2$-$MgCl_2$-DME, respectively.

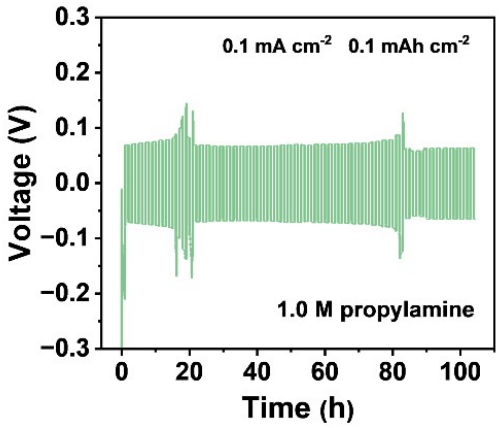


**Figure S19.** Voltage curves of Mg||Mg symmetry cells with the electrolyte adding 1.0 M propylamine.

Propylamine (Alladin, b.p. 48 ℃), an organic monoamine with a relatively high boiling point that remains liquid at room temperature, are selected as the representative case. After dehydration with molecular sieves (Thermo Fisher, 4 Å), it is introduced as an additive into the blank electrolyte, the concentration of which is also 1.0 M. It shows that the electrolyte exhibits excellent electrochemical performance: in Mg||Mg symmetric cell tests, the overpotential at 0.1 mA $cm^{-2}$ and 0.1 mAh $cm^{-2}$ is about 75 mV, which is nearly identical to that of the electrolyte with $Cl^-$ added.

| Without $Cl^-$ | 0 ps | 0.2 ps | 0.5 ps | 1.0 ps |
|---|---|---|---|---|
| NC1(r) | 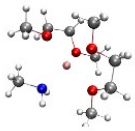 | 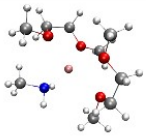 | 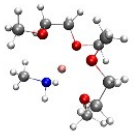 | 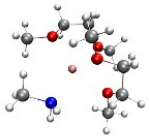 |
| NC2(r) | 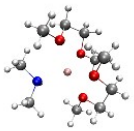 | 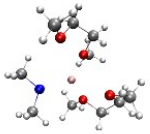 | 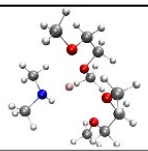 | 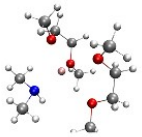 |
| NC3(r) | 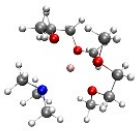 | 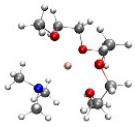 | 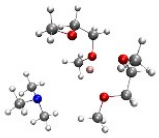 | 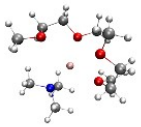 |
| NC4(r) | 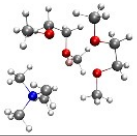 | 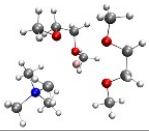 | 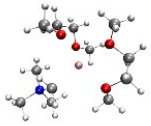 | 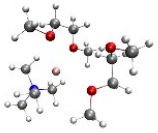 |

**Figure S20.** AIMD of the NC1-NC4 electrolyte without considering the involvement of $Cl^-$.

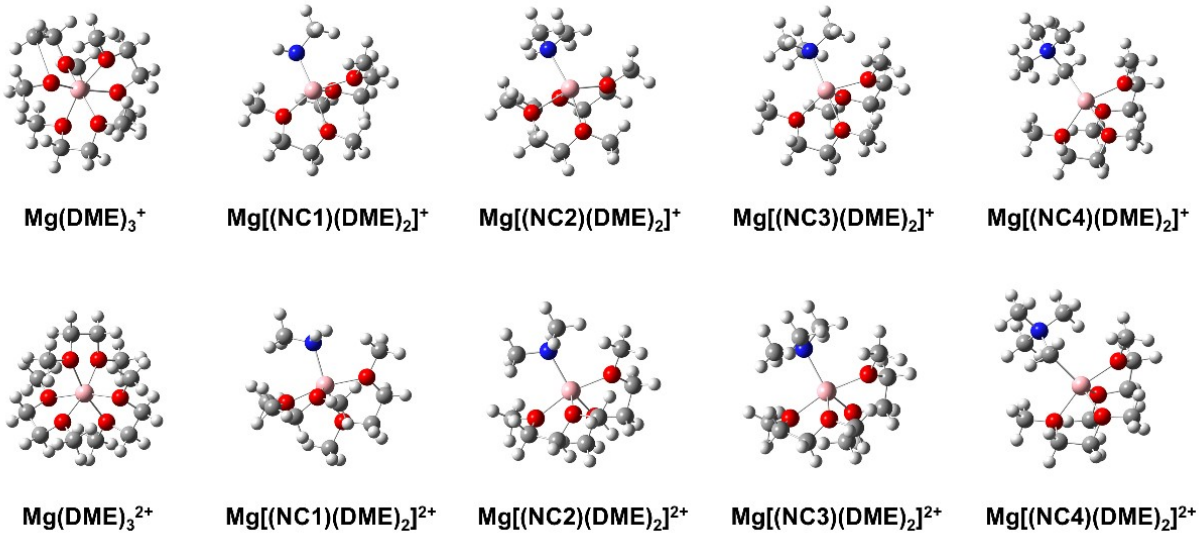


**Figure S21.** The calculated structure of reduced (up) and unreduced (down) solvation sheath. The red, grey, green, blue and white ball represents O, C, Cl, N and H atom, respectively.

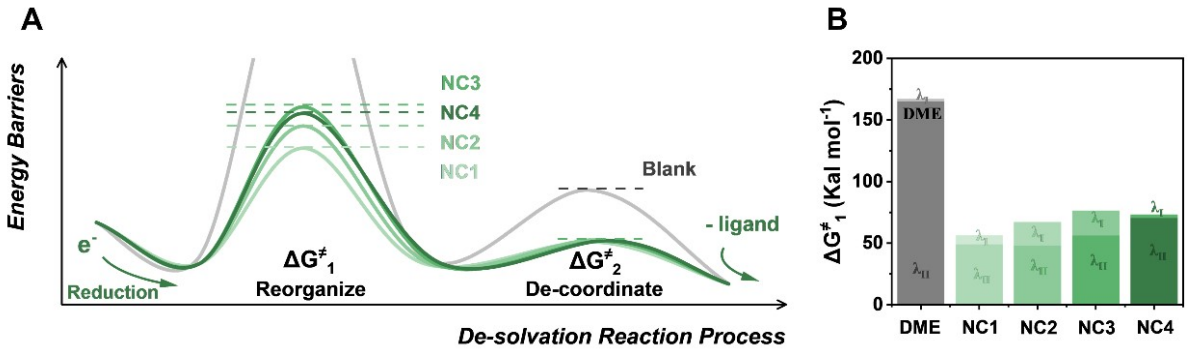


**Figure S22.** When the involvement of $Cl^-$ is not considered, (A) the calculated energy barriers of the de-solvation process reorganization process. (B) detailed energy barrier calculation in the experimental and blank groups.

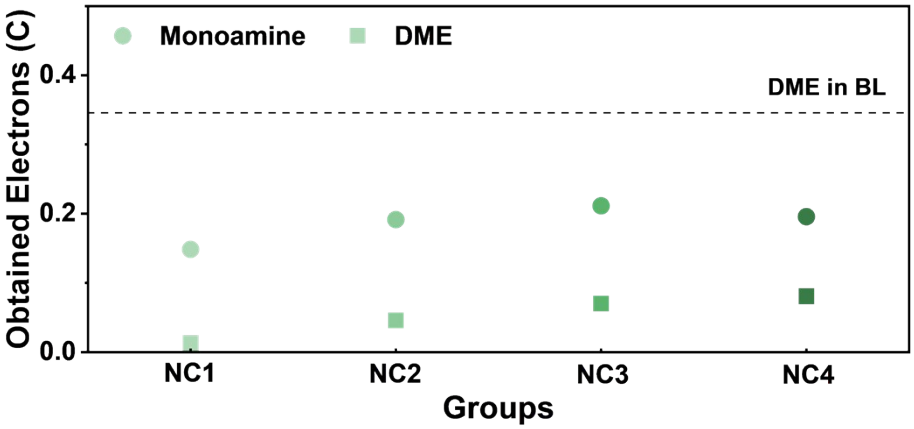


**Figure S23.** When the involvement of $Cl^-$ is not taken into consideration, the calculated obtained electrons of DME molecule and monoamines in the reduction process.

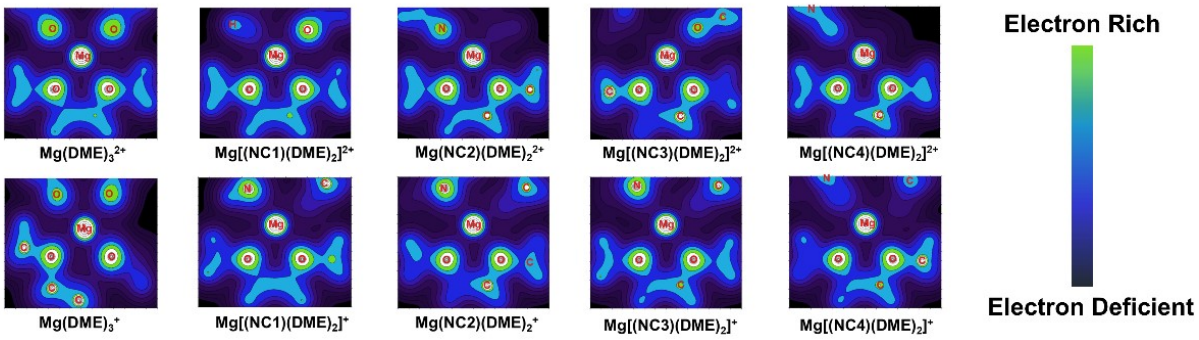


**Figure S24.** Electron density difference plots of the solvation sheath after obtaining a reductive electron in NC1 and the blank group when the involvement of Cl- is not considered. Green parts are the places where reductive electron distribution varies.

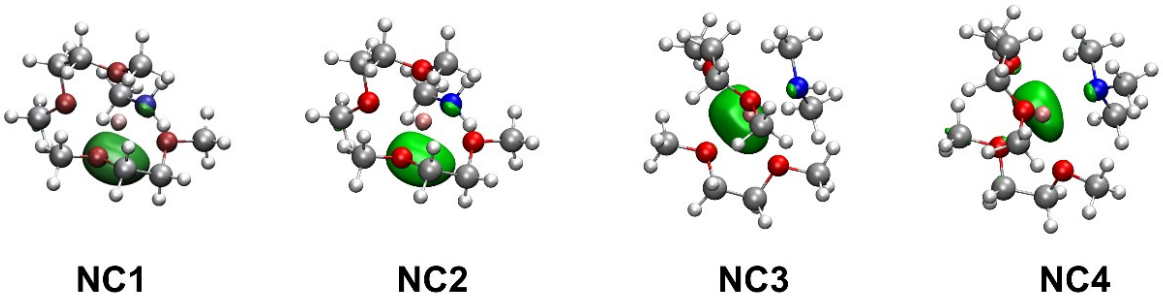


**Figure S25.** When the involvement of $Cl^-$ is not considered, electron density difference plots between reduced/unreduced solvation sheath in (A) NC1, (B) NC2, (C) NC3 and (D) NC4. The red, grey, green, blue and white balls refer to O, C, Cl, N and H atoms, respectively. Green parts are the places where reductive electron distribution varies.

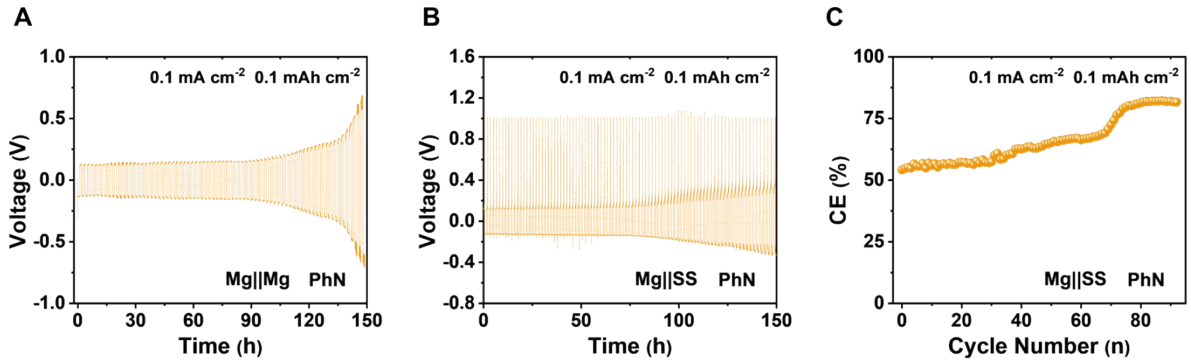


**Figure S26**. (A) The voltage curves of Mg||Mg symmetry cells with the electrolyte of PhN added at 0.1 mA $cm^{-2}$ and 0.1 mAh $cm^{-2}$. (B) The voltage curve of Mg||SS half cells with the electrolyte of PhN added at 0.1 mA $cm^{-2}$. (C) The coulombic efficiency of Mg||SS half cells with the electrolyte of PhN added.

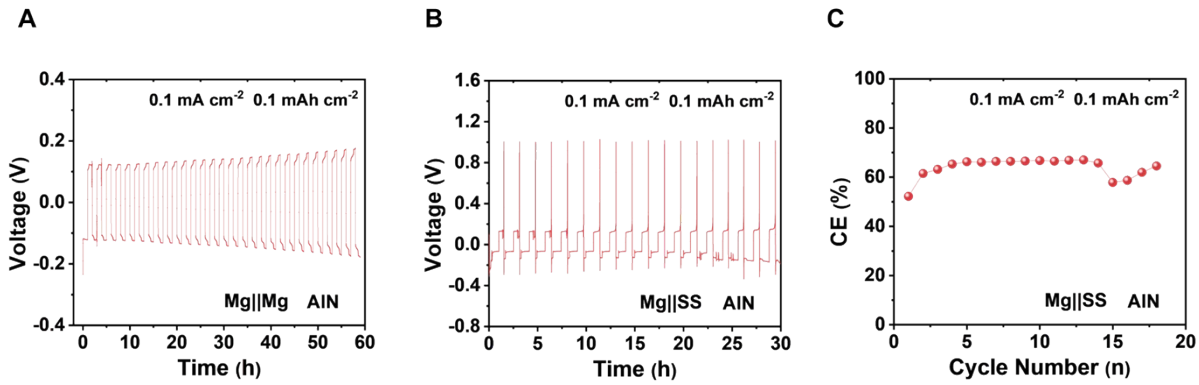


**Figure S27.** (A) The voltage curves of Mg||Mg symmetry cells with the electrolyte of AlN added at 0.1 mA $cm^{-2}$ and 0.1 mAh $cm^{-2}$. (B) The voltage curve of Mg||SS half cells with the electrolyte of AlN added at 0.1 mA $cm^{-2}$. (C) The coulombic efficiency of Mg||SS half cells with the electrolyte of AlN added.

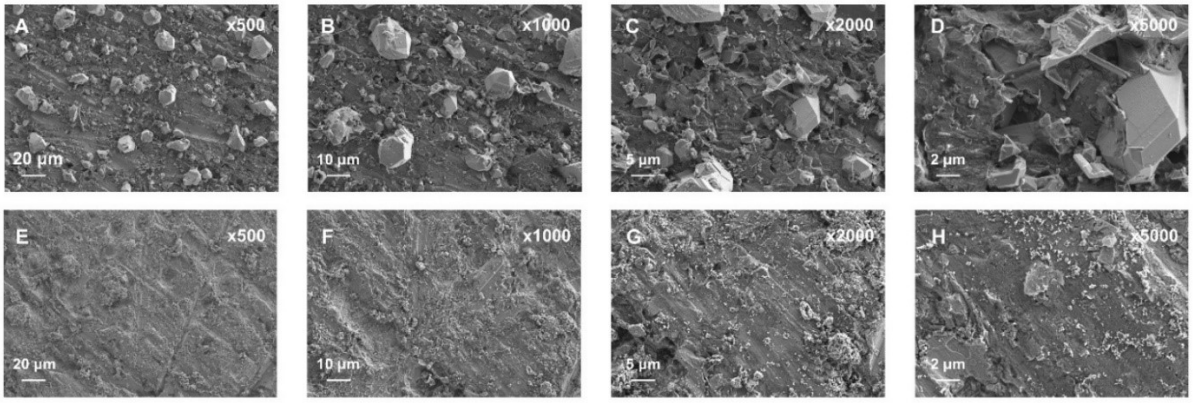


**Figure S28.** SEM images of the Mg anode cycled in blank (A-D) and NC4 electrolyte (E-H) at high current and capacity (1 mA $cm^{-2}$, 3mAh $cm^{-2}$).

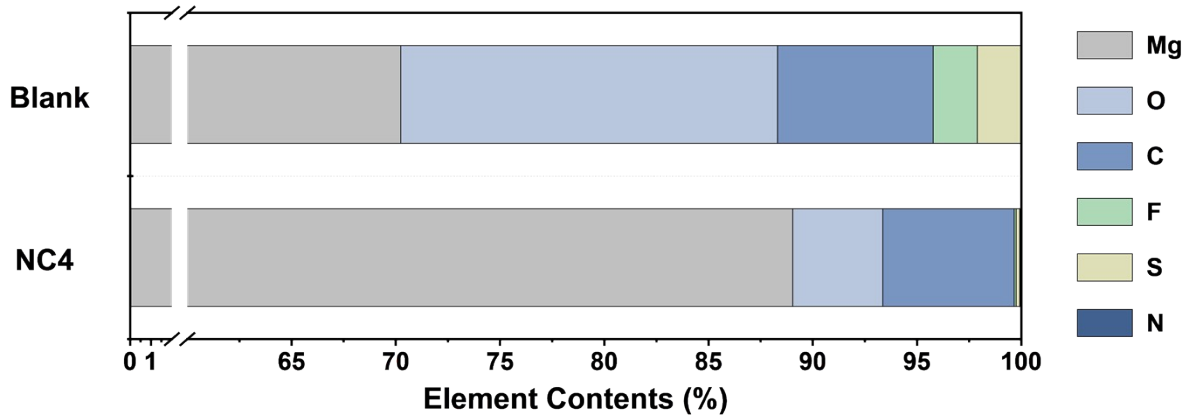


**Figure S29.** Elemental analysis gained by SEM-EDS of the Mg anode after 5 cycles in the blank and NC4 electrolyte. The current and deposition capacity are 1 mA $cm^{-2}$, 3 mAh $cm^{-2}$, respectively.

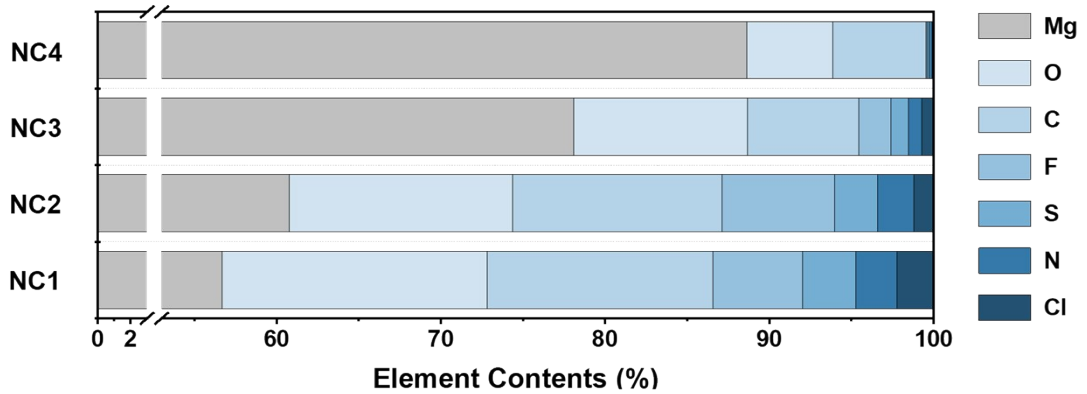


**Figure S30.** Element composition analysis of the surface of Mg anode cycled in the modified electrolytes obtained by scanning electron microscope mapping.

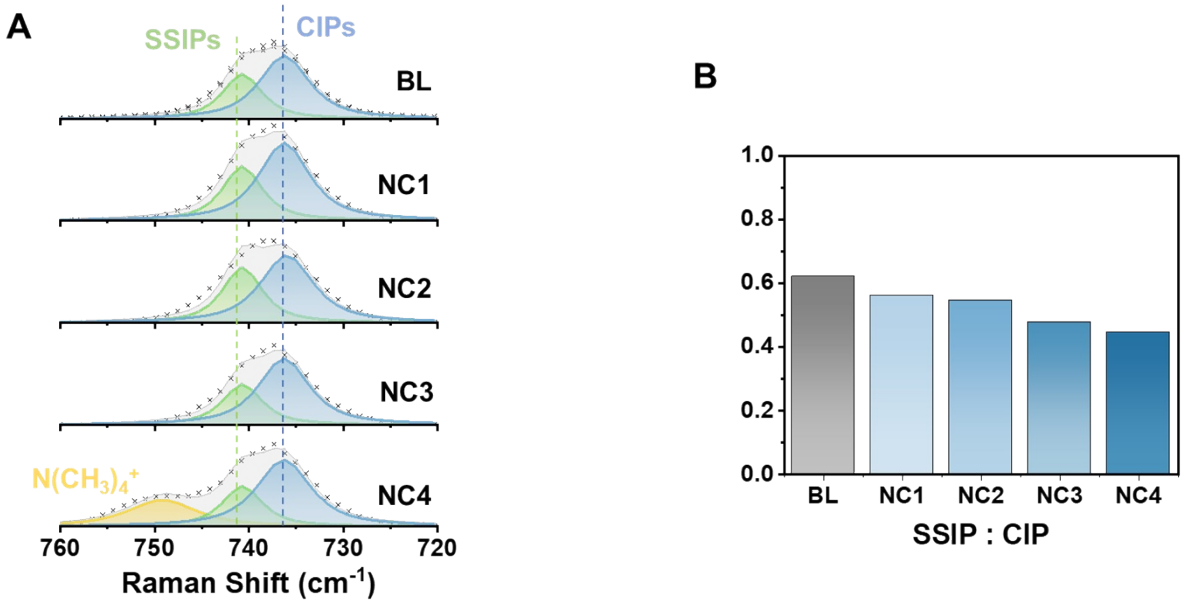


**Figure S31.** (A) Raman spectra of $TFSI^-$ in the blank group and experimental groups. The peaks were plotted and divided into solvent-separated ion pairs (SSIPs), contact ion pairs (CIPs) to investigate their presence percentage. The position and full width at half maxima of the $TFSI^-$ SSIPs Raman peak are 737.6 $cm^{-1}$ and 5.0. (B) The existing form of $TFSI^-$ in different electrolytes calculated according to (A).

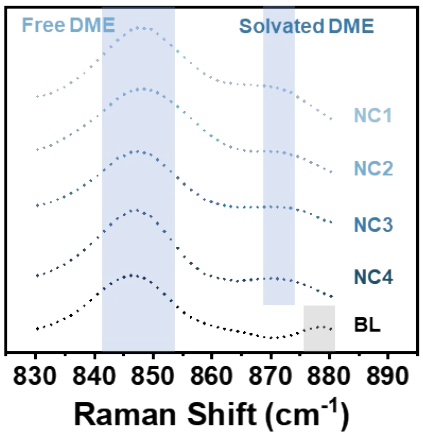


**Figure S32.** Raman spectra of DME molecules in the blank group and experimental groups. The peak that is attributed to free DME molecules remains relatively unchanged, while that representing solvated DME molecules moves to a lower Raman shift in experimental groups, which implies a weakened interaction with $Mg^{2+}$.

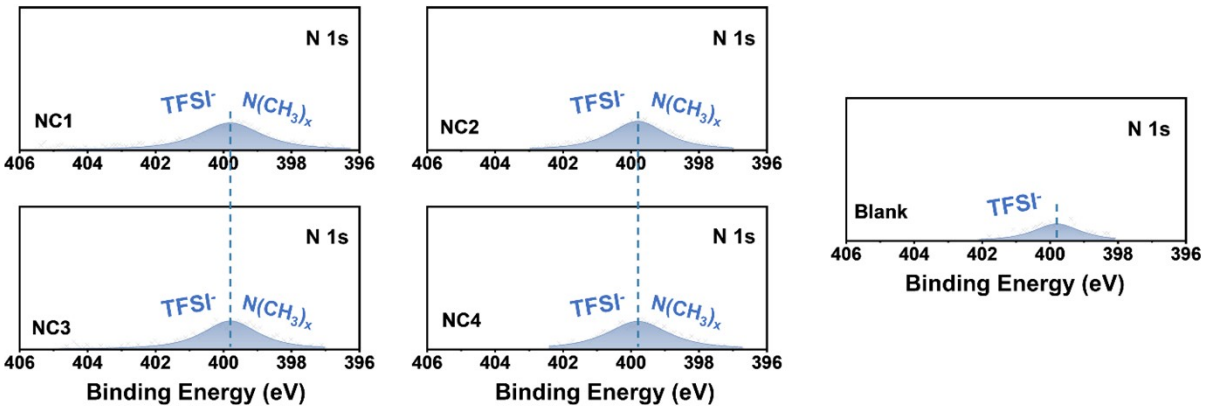


**Figure S33.** The XPS N1s characterization of Mg anode soaked in blank and experimental electrolytes.

It seems that all the electrolytes share the peak of around 399.8 eV, which is ascribed to $TFSI^-$ and $N(CH_3)_x$. The peak of higher binding energy is generated after electrochemical process.

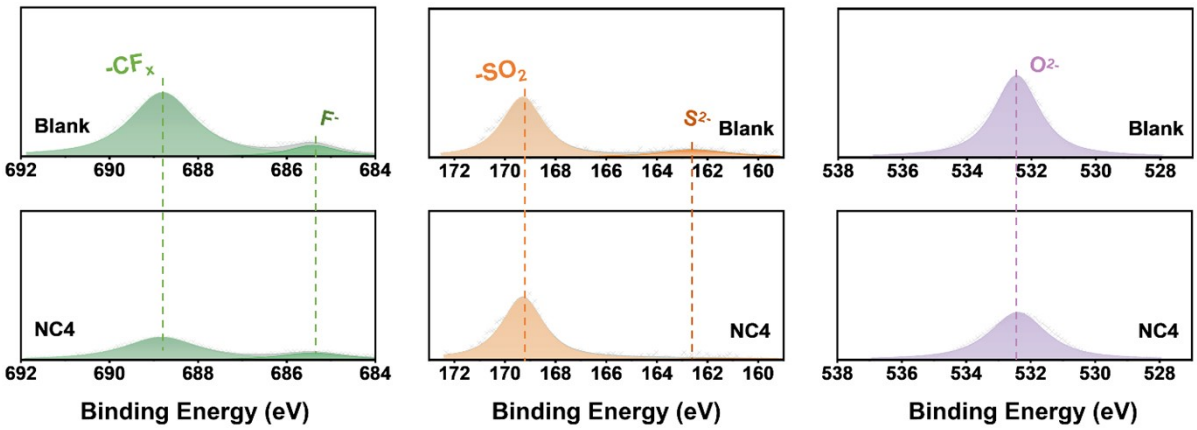


**Figure S34.** The XPS characterization of impurity elements on Mg anode cycled in blank and NC4 electrolyte. The decomposition products have decreased in NC4 electrolytes.

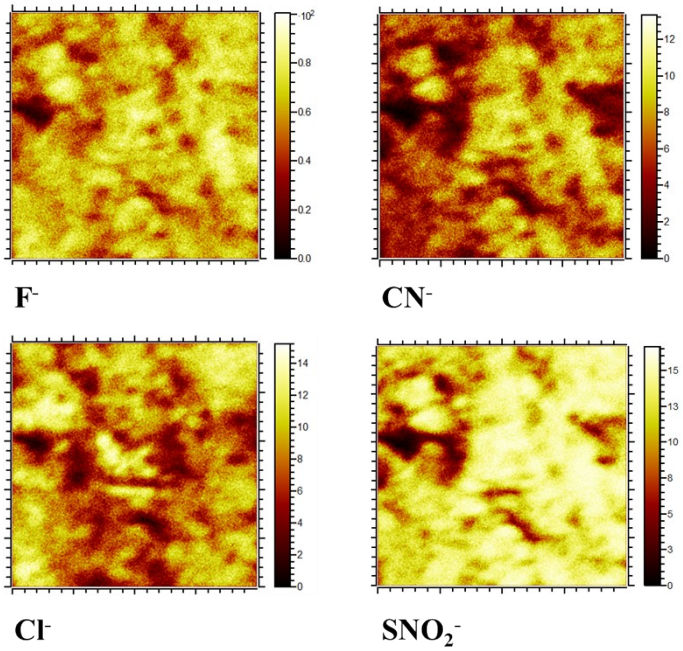


**Figure S35.** Time-of-Flight Secondary Ion Mass Spectrometry mapping results of the Mg anode cycled in NC4 electrolyte.

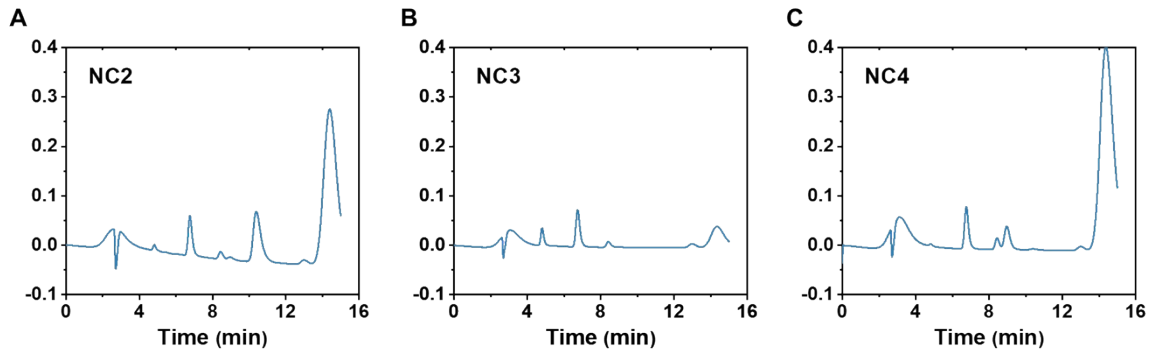


**Figure S36.** Ionic chromatography spectra of the solution which soaks cycled Mg anode in (A) NC2, (B) NC3, and (C) NC4, respectively.

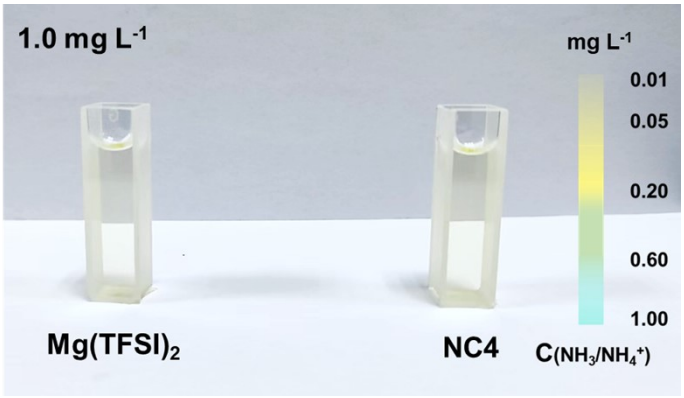


**Figure S37.** Ammonia concentrations tests of the 1.0 mg $L^{-1}$ $Mg(TFSI)_2$-DME and NC4-DME solution by ammonia concentration kit. The unreacted $Mg(TFSI)_2$ and monoamines are examined to cause slight change in solution color.

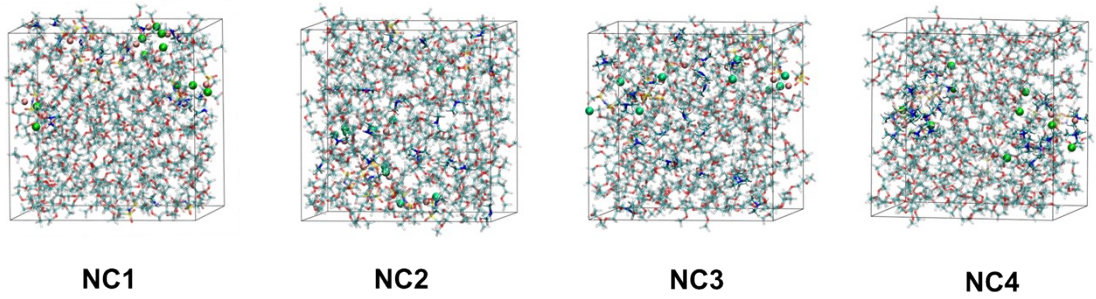


**Figure S38.** The molecule dynamic simulations of experimental groups. The simulation details are described in the Method part.

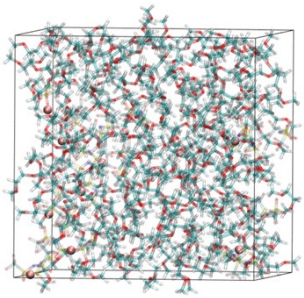

DME

**Figure S39.** The molecule dynamic simulations of the blank group.

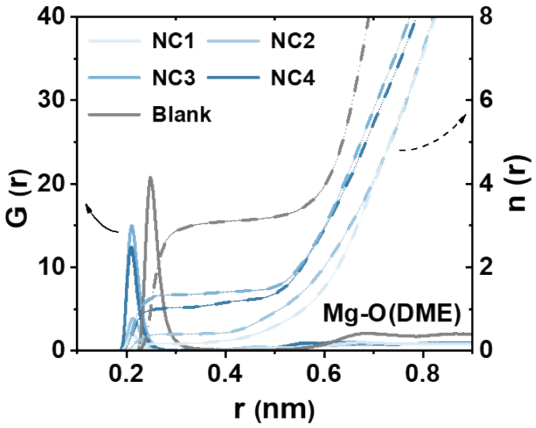


**Figure S40.** Radical distribution function simulations of O in DME in the experimental and blank groups.

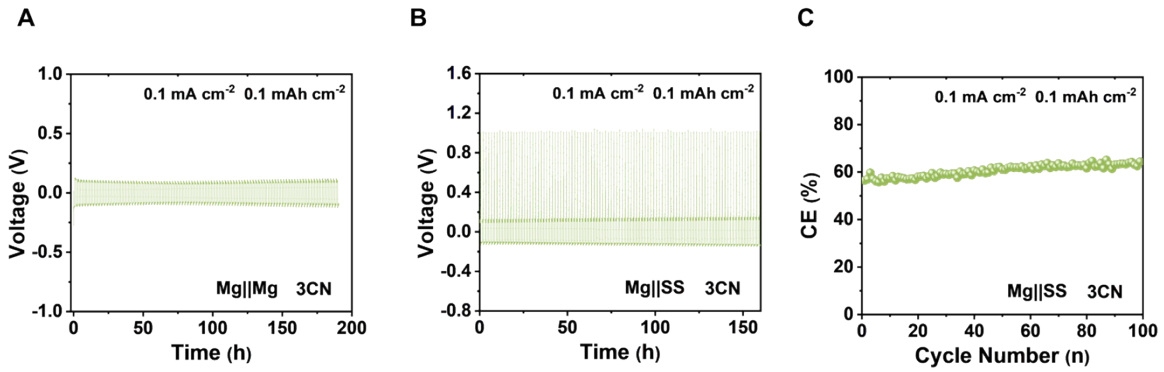


**Figure S41.** (A) The voltage curves of Mg||Mg symmetry cells with the electrolyte of 3CN added at 0.1 mA $cm^{-2}$ and 0.1 mAh $cm^{-2}$. (B) The voltage curve of Mg||SS half cells with the electrolyte of 3CN added at 0.1 mA $cm^{-2}$. (C) The coulombic efficiency of Mg||SS half cells with the electrolyte of 3CN added.

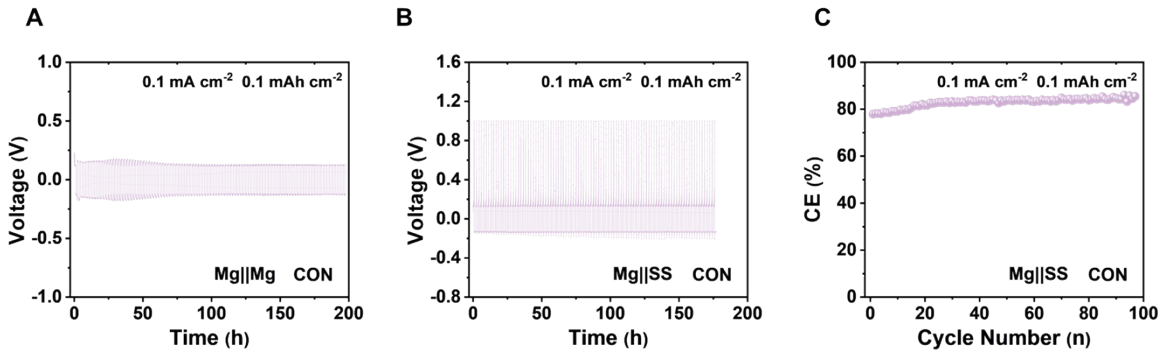


**Figure S42**. (A) The voltage curves of Mg||Mg symmetry cells with the electrolyte of CON added at 0.1 mA $cm^{-2}$ and 0.1 mAh $cm^{-2}$. (B) The voltage curve of Mg||SS half cells with the electrolyte of CON added at 0.1 mA $cm^{-2}$. (C) The coulombic efficiency of Mg||SS half cells with the electrolyte of CON added.

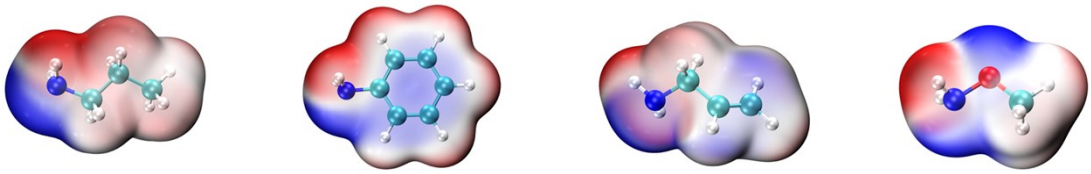

| -46.88 | -40.29 | -42.51 | -35.15 |
|---|---|---|---|
| **3CN** | **PhN** | **AlN** | **CON** |

**Figure S43.** Calculated electrostatic potential plots and the most negative electrostatic potential of monoamine molecules including 3CN, PhN, AlN and CON. The red, grey, blue and white balls refer to O, C, N and H atoms, respectively.

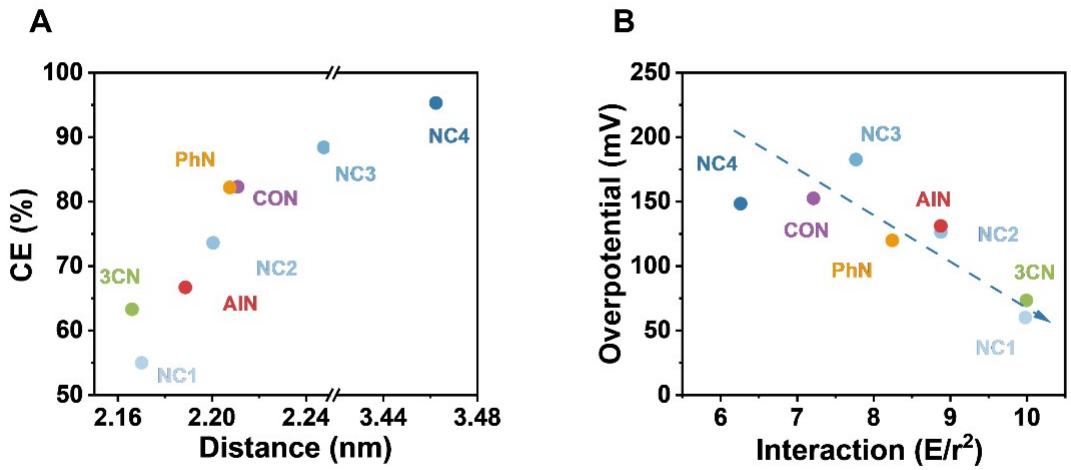


**Figure S44.** When the involvement of $Cl^-$ is not considered, correlation analysis between CE and interaction distance (A), overpotential and the strength (B).

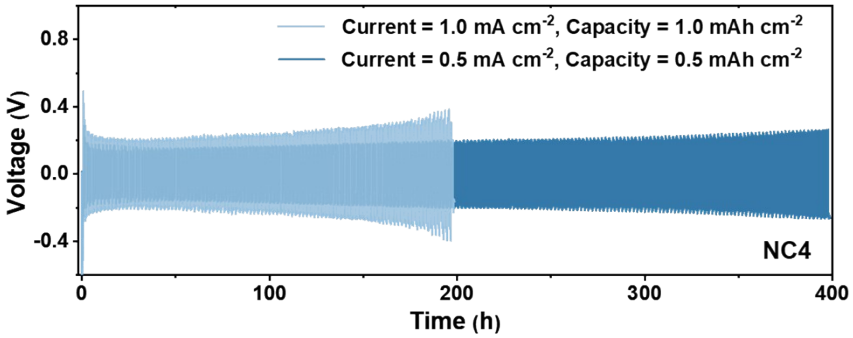


**Figure S45.** The cycling performance of the Mg||Mg symmetry cells with the electrolyte of NC4 at 0.5 mA $cm^{-2}$, 0.5 mAh $cm^{-2}$ (dark blue) and 1.0 mA $cm^{-2}$, 1.0 mAh $cm^{-2}$ (light blue).

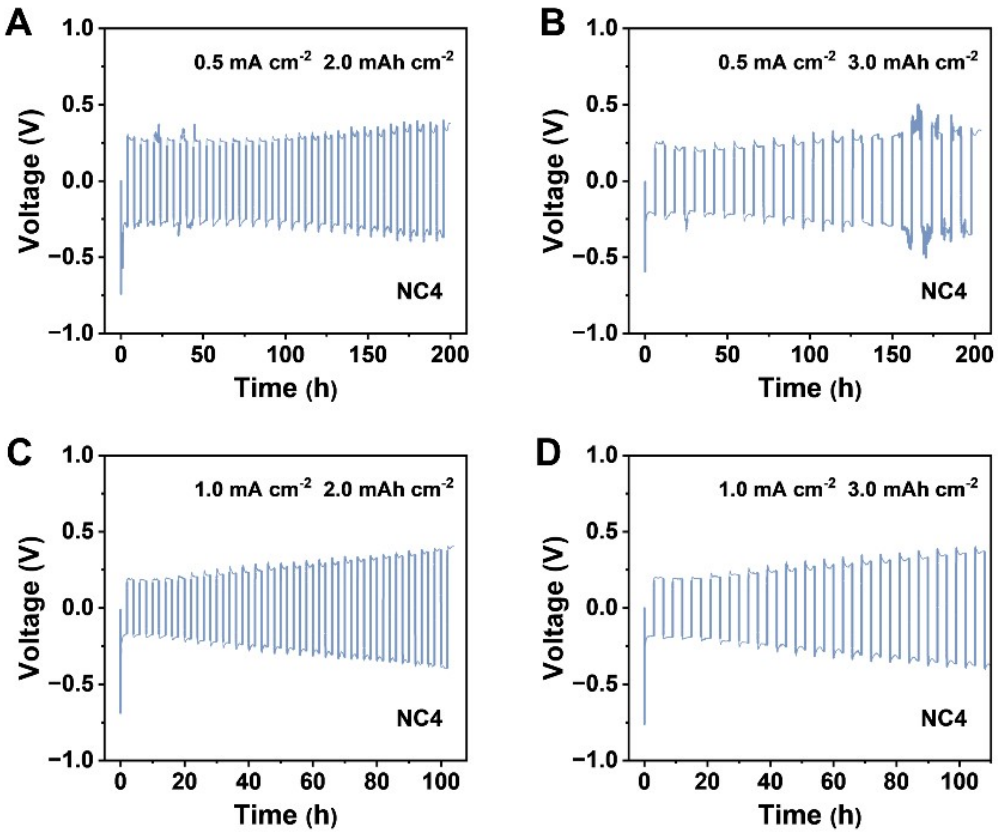


**Figure S46.** The voltage curves of Mg||Mg symmetry cells tested at high current and capacity.

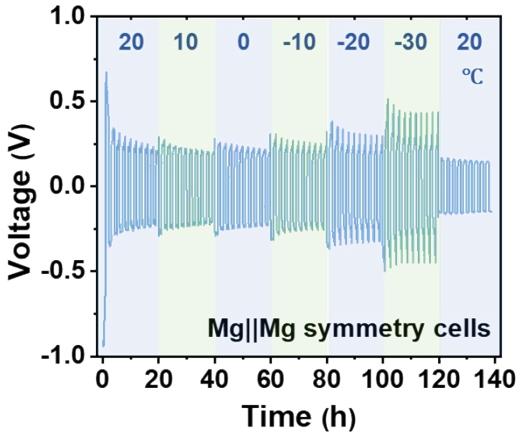


**Figure S47.** The cycling performance of the Mg||Mg symmetry cells with the electrolyte of NC4 at low temperatures (from 20 ℃ to -30 ℃) at 0.1 mA $cm^{-2}$, 0.1 mAh $cm^{-2}$.

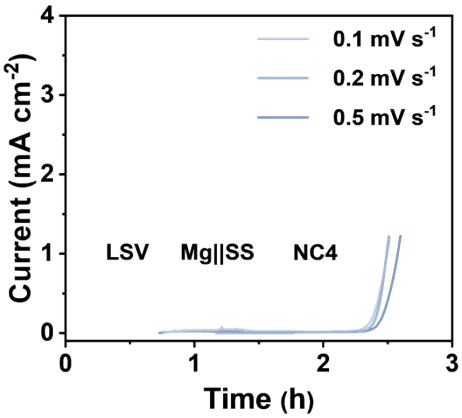


**Figure S48**. LSV test of Mg||SS half cells at different scanning rates.

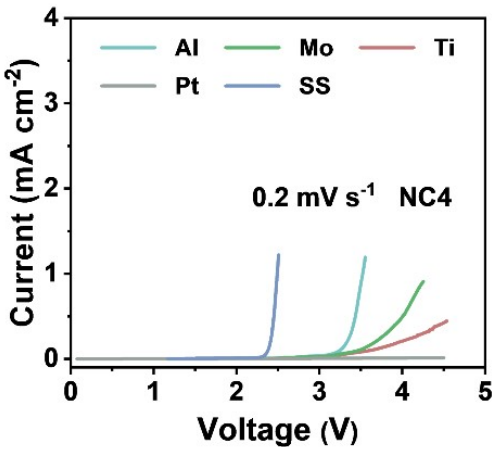


**Figure S49.** LSV test of Mg half cells at different current collectors.

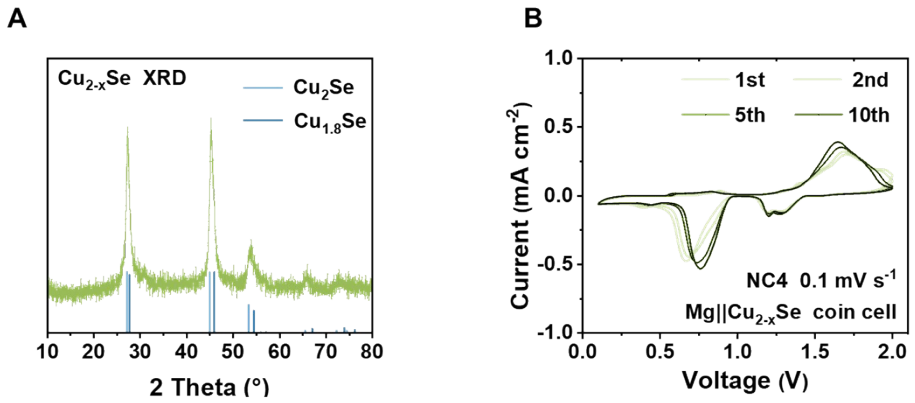


**Figure S50.** (A) XRD spectra of the as-prepared $Cu_{2-x}Se$ cathode. (B) CV curves of Mg||$Cu_{2-x}Se$ cells tested at 0.1 mV $s^{-1}$.

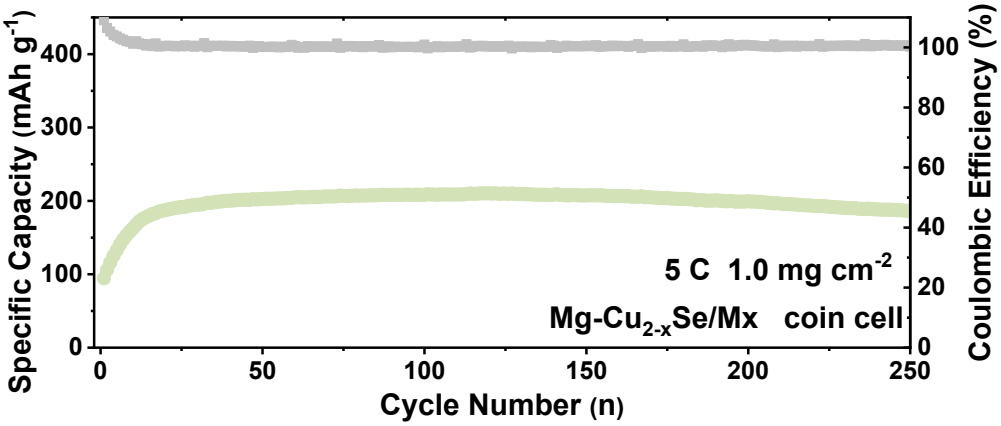


**Figure S51.** Cycling performance of Mg||$Cu_{2-x}Se$ cathode full cell in coin cells at the current of 5 C.

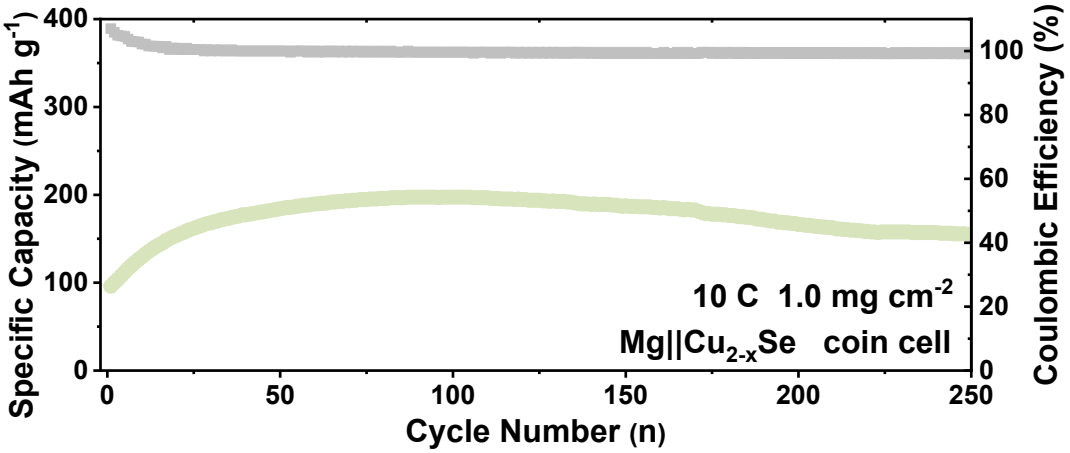


**Figure S52.** Cycling performance of Mg||$Cu_{2-x}Se$ cathode full cell in coin cells at the current of 10 C.

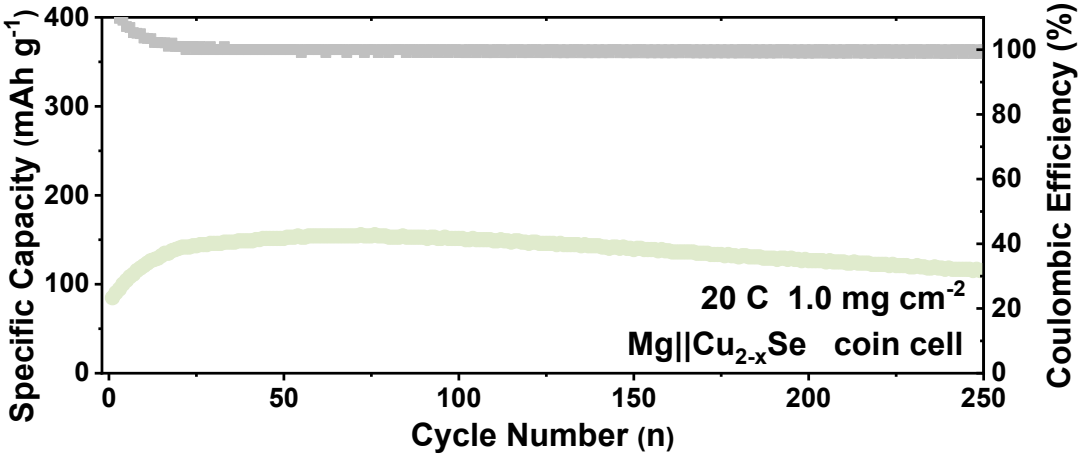


**Figure S53.** Cycling performance of Mg||$Cu_{2-x}Se$ cathode full cell in coin cells at the current of 20 C.

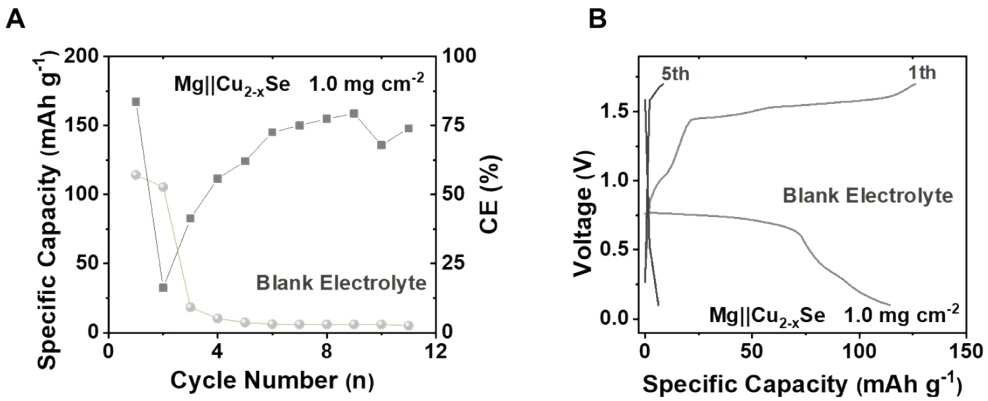


**Figure S54.** (A) Cycling performance and (B) voltage profiles of the Mg||$Cu_{2-x}Se$ cells with NC4 and blank electrolyte.

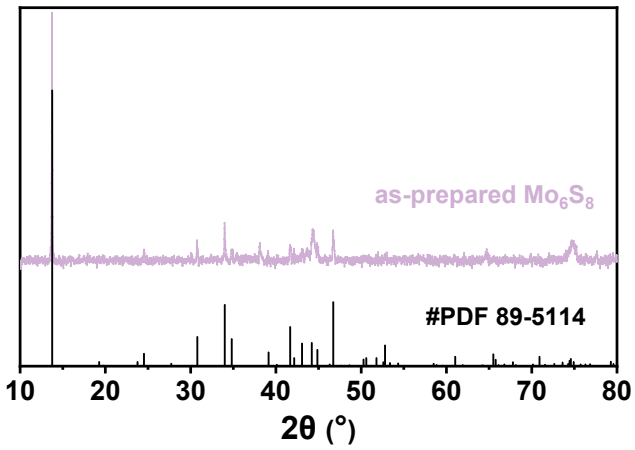


**Figure S55.** XRD spectra of the as-prepared $Mo_6S_8$ nanoplate cathode.

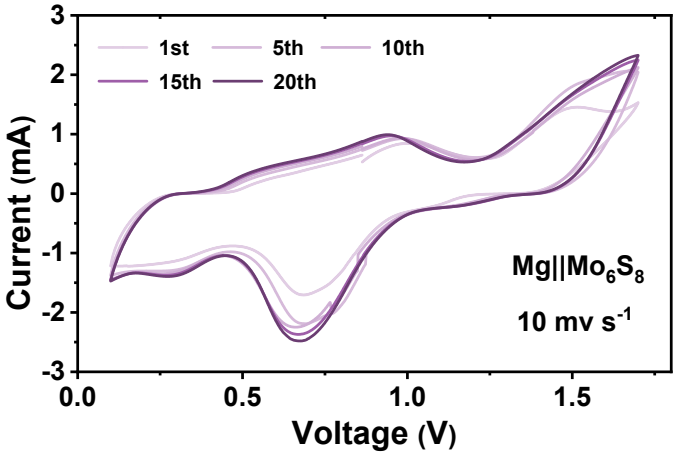


**Figure S56.** CV curves of Mg||$Mo_6S_8$ coin cell tested at 0.1 mV $s^{-1}$.

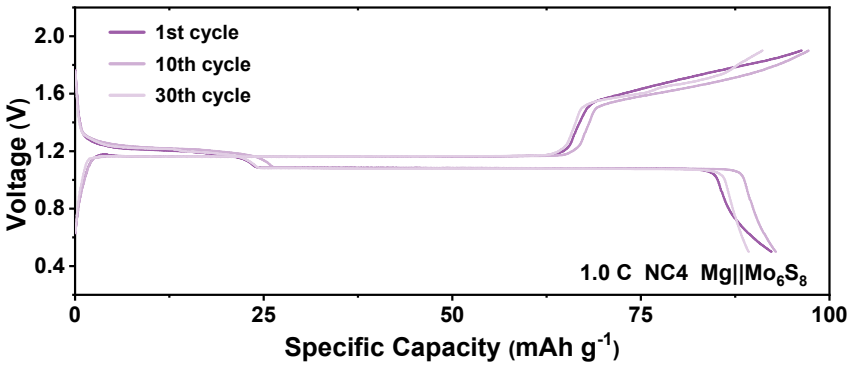


**Figure S57.** Voltage profiles of the Mg||$Mo_6S_8$ coin cells with the NC4 electrolyte at various cycles.

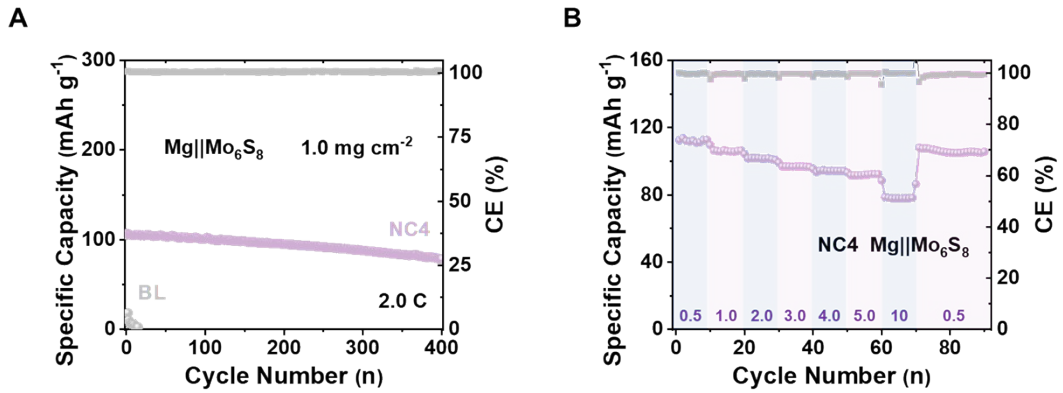


**Figure S58.** (A) Cycling performance of Mg||$Mo_6S_8$ coin cells with NC4 and blank electrolyte. (B) Rate performance of the Mg||$Mo_6S_8$ coin cells with the NC4 electrolyte, the current of which ranges from 0.5 C to 10 C.

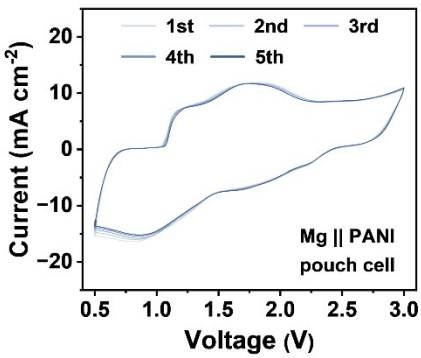


**Figure S59.** Cyclic voltammetry curves of Mg||PANI Swagelok cells tested at 1 mV $s^{-1}$.

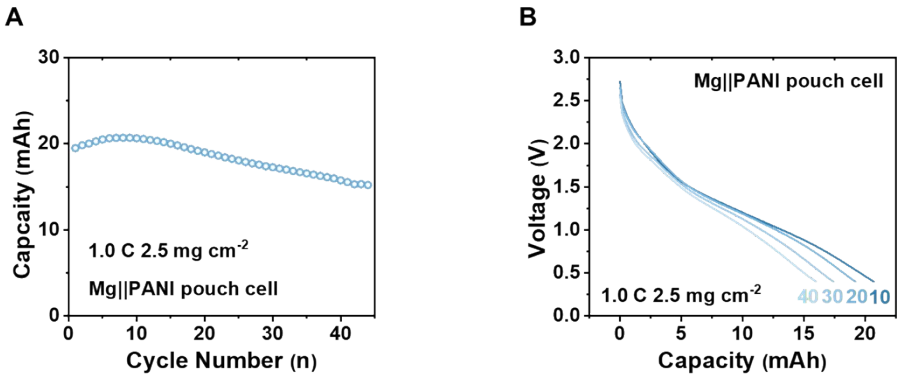


**Figure S60.** (A) Cycling performance and (B) discharging voltage curves of the Mg||PANI pouch cells with high area loading (2.5 mg $cm^{-2}$) at the current of 1.0 C.

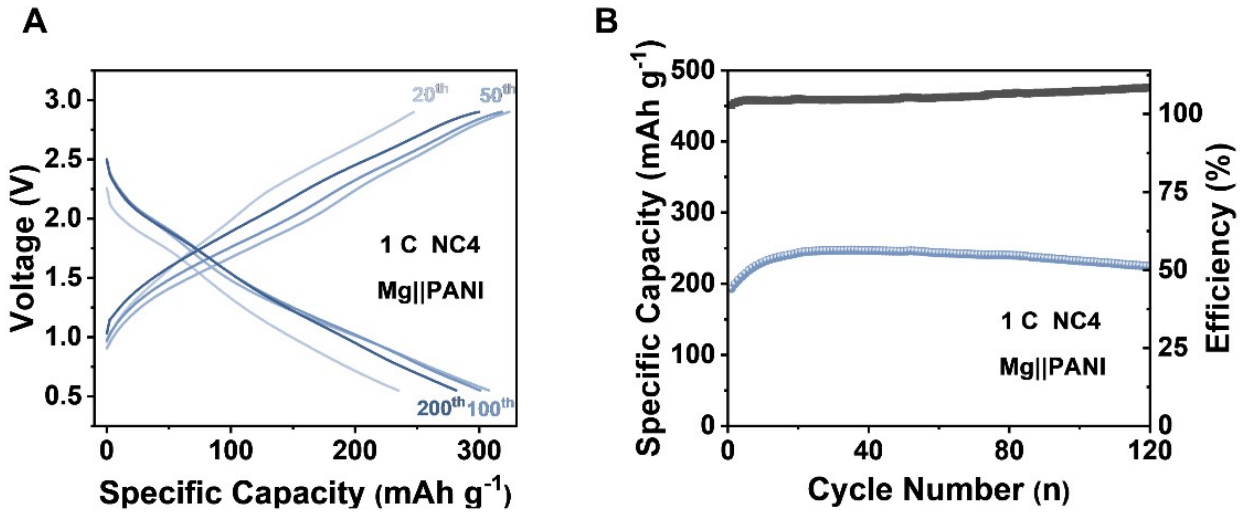


**Figure S61.** (A) Voltage curves and (B) cycling performance of Mg||PANI pouch cells at 1 C.

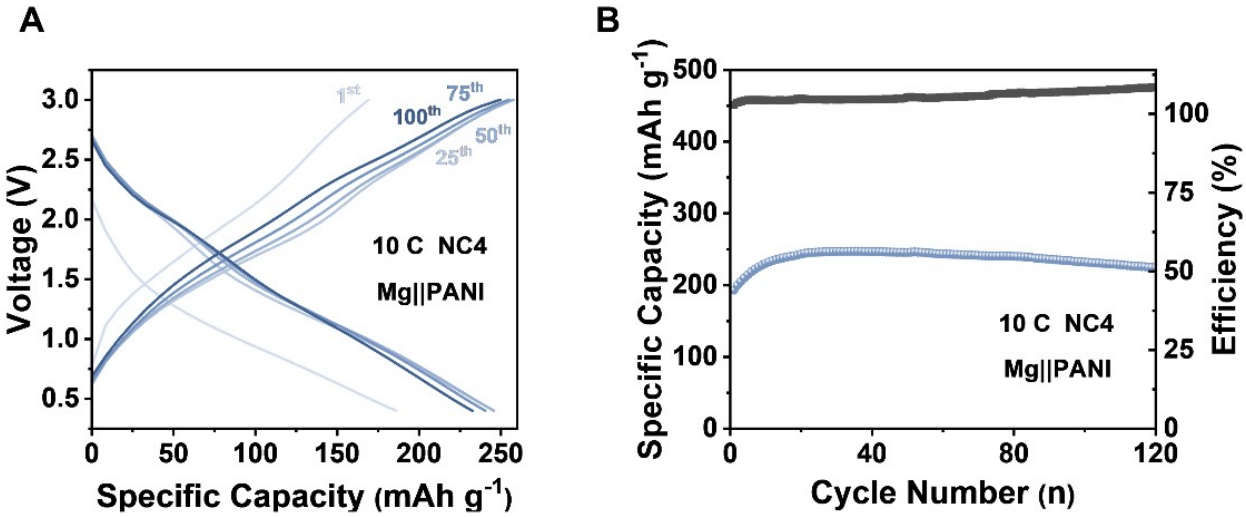


**Figure S62.** (A) Voltage curves and (B) cycling performance of Mg||PANI pouch cells at 10 C.

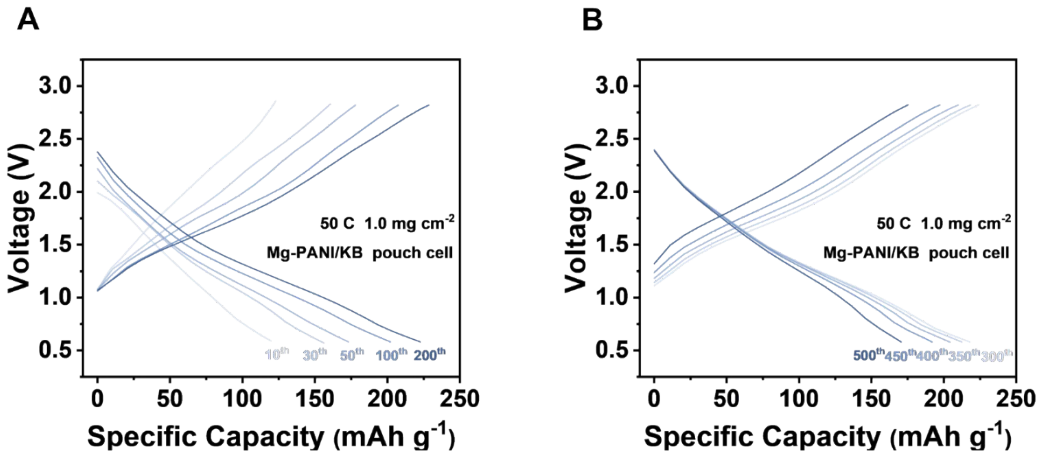


**Figure S63.** Voltage curves of the initial cycles (A) and decay cycles (B) in the Mg||PANI pouch cells at a current density of 50 C.

In initial cycles, due to the electrolyte conditioning and cathode refinement, the polarization decreases and the specific capacity increases. On the contrary, in the decay cycles, due to irreversible oxidation side reactions accompanied by structural degradation of the PANI backbone, the polarization increases and the cycling stability is not that satisfactory.

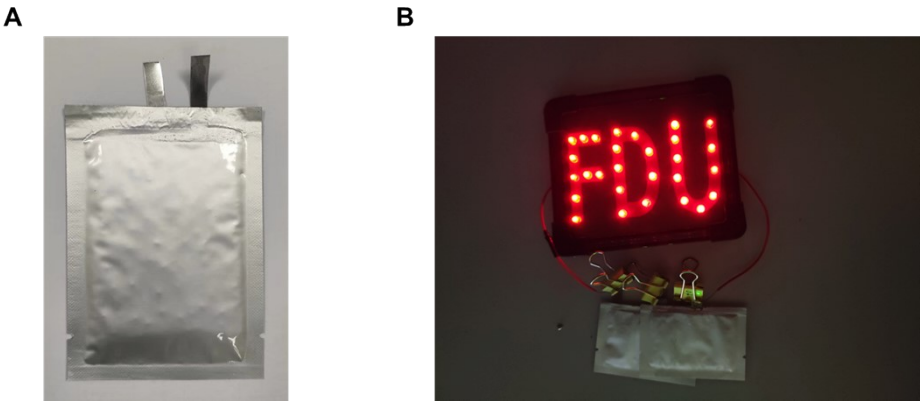


**Figure S64.** (A) The images of the sample prototype Mg||PANI pouch cell with the electrolyte of NC4. (B) LED light bulbs are lit by pouch cells. Two pouch cells are needed because the rated voltage of LED bulbs is 3.5 V.

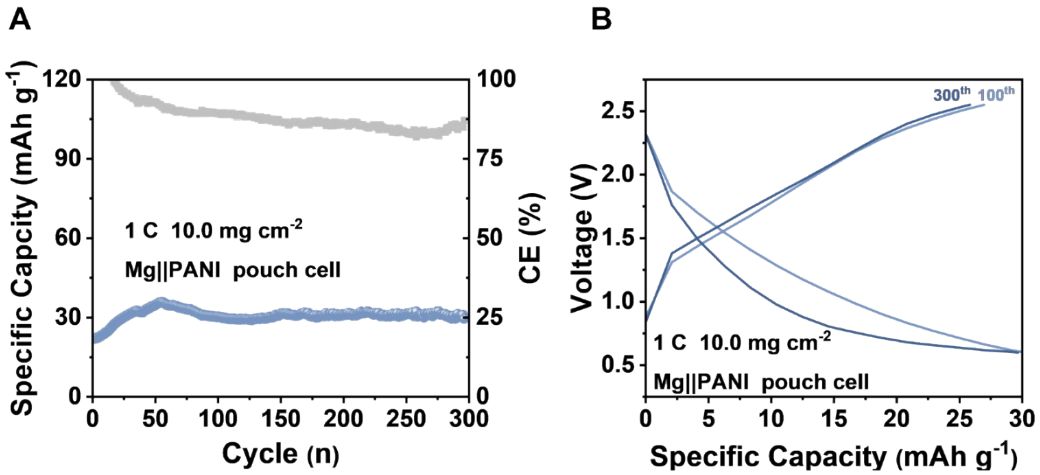


**Figure S65.** The cycling performance (A) and voltage profiles of Mg||PANI pouch cells with PANI loading of 10 mg $cm^{-2}$.

There is no carbon material in the cathode. It demonstrates that the modified electrolyte can support the operation of cathodes with high mass loadings.

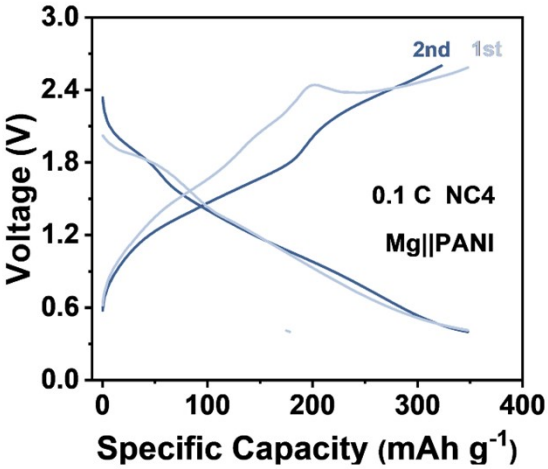


**Figure S66.** Voltage curves and of Mg||PANI pouch cells at 0.1 C.

**Table S1.** Binding energy of different potential solvation sheath structures in NC1 electrolyte. For simplicity, in the table, **C**, **N** and **D** represents $Cl^-$, NC1 and DME.

| Unit: Kcal $mol^{-1}$ | 1C1N2D | 2N2D | 3D | 1Cl3N1D | 4N1D |
|---|---|---|---|---|---|
| **Binding Energy** | -175.1 | -150.0 | -143.1 | — | — |

Besides, "—" indicates that the corresponding solvation sheath structure is not stable. NC1 are selected as the representative for binding energy calculation because it has the smallest steric hindrance among all organic monoamines, and is therefore most likely to enter the solvation sheath of $Mg^{2+}$. In contrast, for monoamines with larger steric hindrance, NC3 and NC4 for instance, it is difficult for multiple organic amine molecules to coordinate with $Mg^{2+}$ simultaneously in the solvation sheath. It should be noted that the entire solvation sheath is positively charged, so at most one $Cl^-$ can be present. In addition, the overall coordination number of the $Mg^{2+}$ solvation sheath should be six. According to the calculation results, $[MgCl(NC1)(DME)_2]^+$ should be the most possible structure.

**Table S2.** The calculated binding energy of different solvation sheath structure before and after the reduction in Figure S4.

| Unit: Kcal $mol^{-1}$ | Reduced | Unreduced |
|---|---|---|
| $[MgCl(NC1)(DME)_2]^{n+}$ | -175.1 | -78.1 |
| $[MgCl(NC2)(DME)_2]^{n+}$ | -172.7 | -71.6 |
| $[MgCl(NC3)(DME)_2]^{n+}$ | -173.5 | -76.4 |
| $[MgCl(NC4)(DME)_2]^{n+}$ | -184.9 | -72.8 |
| $[Mg(DME)_3]^{n+}$ | -143.2 | -47.2 |
| $[MgCl(DME)_2]^{n+}$ | -150.0 | -73.0 |

**Table S3.** Average strain energy of DME molecules in reduced/unreduced electrolytes. The energy of DME molecule is calculated as $E_{DME}$, and $E_{strain} = \sum_{1}^{n}(E_n - E_{DME})/n$.

| $E_{strain}$ (kcal mol$^{-1}$) | Reduced | Unreduced |
|---|---|---|
| **Blank** | 38.71 | 0.96 |
| **NC1** | 2.90 | 1.57 |
| **NC2** | 3.05 | 3.88 |
| **NC3** | 2.45 | 4.02 |
| **NC4** | 2.61 | 2.78 |

**Table S4.** Energy barriers of the reorganization and de-coordination process in experimental and blank electrolytes displayed in Figure 2A and Figure S20.

| **Unit: Kcal mol$^{-1}$** | **Blank** | **NC1** | **NC2** | **NC3** | **NC4** |
|---|---|---|---|---|---|
| $\Delta G_1^{\neq}$ | 166.3 | 38.8 | 40.3 | 55.6 | 54.1 |
| $\Delta G_2^{\neq}$ | 49.9 | 21.3 | 24.8 | 37.0 | 29.4 |
| $\Delta G_1^{\neq}$ (no Cl$^-$) | 166.3 | 56.2 | 67.0 | 76.3 | 73.2 |
| $\Delta G_2^{\neq}$ (no Cl$^-$) | 35.7 | 10.5 | 11.4 | 10.8 | 11.1 |

**Table S5**. Calculated ionic conductivity (σ) and ohmic polarization ($\eta_{ohmic}$) of the blank and experimental electrolytes.

| | $R_b$ (Ohmic) | Ionic conductivity ($mS \cdot cm^{-1}$) | Ohmic polarization (mV) |
|---|---|---|---|
| **Blank** | 125.3 | 0.135 | 9.84 |
| **NC1** | 6.8 | 2.50 | 0.53 |
| **NC2** | 10.6 | 1.59 | 0.83 |
| **NC3** | 13.8 | 1.23 | 1.08 |
| **NC4** | 16.7 | 1.02 | 1.31 |

$$\sigma = \frac{L}{A \cdot R_b}, \quad \eta_{ohmic} = \frac{I \cdot L}{\sigma \cdot A}$$

σ, L, A, I, $\eta_{ohmic}$ and $R_b$ represent the ionic conductivity, thickness of separator (0.03 cm), electrode area (0.785 $cm^2$), current (0.0785 mA), ohmic polarization and X-axis resistance, respectively.

**Table S6.** Summary of calculated $\Delta G_1^{\neq}, r, -E$ and experimented λ, CE of all the experimental groups.

| | **NC1** | **NC2** | **NC3** | **NC4** | **CON** | **PhN** | **AlN** | **3CN** |
|---|---|---|---|---|---|---|---|---|
| $\Delta G_1^{\neq}$ | 38.77 | 40.30 | 55.62 | 54.14 | 55.33 | 48.60 | 45.20 | 39.12 |
| ***r* (nm)** | 2.17 | 2.20 | 2.24 | 3.46 | 2.21 | 2.21 | 2.19 | 2.17 |
| ***-E*** | 46.99 | 42.98 | 39.24 | 75.06 | 35.15 | 40.29 | 42.51 | 46.88 |
| $-E/r^2$ | 9.98 | 8.88 | 7.77 | 6.26 | 7.21 | 8.24 | 8.34 | 8.87 |
| **$\lambda$(mV)** | 60.1 | 126.4 | 182.6 | 148.4 | 152.5 | 119.9 | 131.1 | 73.4 |
| **CE** | 55% | 74% | 88% | 96% | 82% | 83% | 67% | 63% |

$\Delta G_1^{\neq} = abs(E_{11} + E_{12}) + abs(E_{21} + E_{22})$. The $r$ refers to the interaction distance between N and $Mg^{2+}$, while $E$ refers to the calculated electrostatic potential of different monoamines.

**Table S7**. The X-ray Photoelectron Spectroscopy Peak position in Fig. 2a. All the spectroscopy spectra are adjusted with $C_{1s}$ peak.

| | $C_{1s}$ | $N_{-TFSI^-}$ | $N_{-NH+}$ |
|---|---|---|---|
| **Peak position (eV)** | 288.8 | 399.8 | 402.1 |

**Table S8**. Mass of all components of a sample Mg pouch cell.

| | **Mass (mg)** |
|---|---|
| **Cathode Material** | 58.9 |
| **Mo mesh** | 521.1 |
| **GF/F** | 219.9 |
| **Mg foil** | 83.0 |
| **Electrolyte** | 1178.2 |
| **Al Foil Casing** | 1068.4 |

**Table S9.** The cathode material, current, specific capacity, energy density and power density of the cited studies in Fig. 4g.

| Citation | Cathode material | Current (mA $g^{-1}$) | Capacity (mAh $g^{-1}$) | Energy density (Wh $kg^{-1}$) | Power density (W $kg^{-1}$) |
|---|---|---|---|---|---|
| [43] | CuS | 5 | 400.0 | 608.0 | 8.0 |
| [43] | CuS | 50.0 | 252.0 | 335.2 | 67.0 |
| [43] | CuS | 100.0 | 194.0 | 230.9 | 119.0 |
| [11] | CuS | 29.4 | 89.0 | 90.8 | 30.0 |
| [45] | PM-$Mo_6S_8$ | 62.5 | 85.0 | 80.0 | 58.8 |
| [46] | $CoS_x$ | 40.0 | 152.0 | 153.5 | 40.4 |
| [47] | NCSe@TiVC | 100.0 | 104.0 | 111.3 | 107 |
| [48] | $Mo_6S_8$ | 37.5 | 59.0 | 57.8 | 36.8 |
| [49] | $FeSe_2$ | 200.0 | 217.4 | 260.9 | 147.0 |
| [50] | $Mo_6S_8$ | 25.0 | 112.0 | 204.0 | 45.5 |
| [51] | S | 335.0 | 530.0 | 551.2 | 348.4 |
| [52] | $Mo_6S_8$ | 62.5 | 47.0 | 47.5 | 63.1 |
| [53] | $MoS_3$ | 20.0 | 290.2 | 278.6 | 19.2 |
| [54] | $Mo_6S_8$ | 12.5 | 19.5 | 18.7 | 12.0 |

The energy density and power density are estimated and calculated based on the discharging curves if these data are not included in their supplementary information.

**Table S10.** Energy and power density of the 50 C pouch cell calculated based on different standards.

| Based on | Energy density (Wh $kg^{-1}$) | Power density (W $kg^{-1}$) |
|---|---|---|
| **Cathode** | 266.6 | 16016 |
| **Cathode and anode** | 110.7 | 6647.9 |
| **Cathode, anode and electrolyte** | 11.89 | 714.59 |
| **The whole pouch cell** | 5.018 | 301.44 |

**Table S11.** The comparison of Mg pouch cells' energy density and power density calculated based on the mass of cathode and anode between this work and previous research.

| Cathode material | Energy density (Wh $Kg^{-1}$) | Power density (W $Kg^{-1}$) |
|---|---|---|
| **PANI (This work, 10 C)** | 110.7 | 6647.9 |
| **PANI (This work, 50 C)** | 180.0 | 1315.6 |
| **$Mg_{0.15}MnO_2$**[24] | 412.0 | ~228.9 |
| **CuS**[11] | 666.5 | ~291.0 |
| **$FeSe_2$**[49] | 45.1 | ~201.9 |
| **PM-$Mo_6S_8$**[45] | 80.0 | ~65.7 |